

Aerodynamic interaction of two neighbouring offshore wind farms in a conventionally neutral boundary layer, for varying wind farm distances



(Energy Watch, 2022)

Master's Thesis

by

Jasper van Asselt

Date of Submission: February 15, 2025

Committee:

First examiner:
Assistant prof. dr. J.O. Colomes Gene

Second examiner:
Prof. dr. S.J. Watson

Supervisors:
Ir. M.A. Khan
Dr. S.P. Porchetta

External Supervisor Witteveen+Bos:
Ir. B. Gradussen

Preface

This report is the last step into obtaining my Master of Science in Civil Engineering (track: Hydraulic and Offshore Structures) at Delft University of Technology. I have decided to do my MSc thesis in collaboration with the faculty of Aerospace due to my interest in all processes related to offshore structures. Furthermore, I am greatly interested in innovation and this led me to the topic of aerodynamic interaction of two neighbouring offshore wind farms. After submitting this thesis, I hope to have contributed to the development of offshore wind farms, and hope that this is not the last step I will make in this field.

I want to thank Witteveen+Bos for showing interest in my thesis topic and helping me along the way. I enjoyed the time at the offices with my colleagues. It helped me a lot in making decisive choices. A special thanks to Bas and Daniel for giving feedback and collaborating with me on ideas. Then my gratitude also goes to my committee: Mehtab, Simon, Oriol and Sara. I felt part of the small research community, and really enjoyed to write an abstract about this thesis for WindEurope 2025. Special thanks to Mehtab for spending hours with me.

Finally, I would like to thank my family and friends in Delft and Utrecht. I always felt included, even though I did not live in Delft. Special thanks to my amazing parents, Sandra and André, for always believing in me. And my smart sister Lisa, for being my spar-maatje. My final thanks goes to Niki, for being proud every small step I made. Thank you all!

J. (Jasper) van Asselt
Delft, February 2025

Abstract

This study investigates the aerodynamic interaction between two neighbouring offshore wind farms operating in a Conventionally Neutral Boundary Layer (CNBL), where the atmospheric boundary layer (ABL) is neutrally stable, capped by a stable inversion layer and a less stable free atmosphere above. While previous studies have investigated: 1) wake effects between two neighbouring wind farms in a Truly Neutral Boundary Layer (TNBL) with neutral conditions throughout the ABL and above, and 2) the impact of a single wind farm on the flow field in a CNBL, there is a lack of research on the interaction between neighbouring wind farms in a CNBL. Improving our understanding of wind farm interactions in a realistic atmosphere is important for offshore wind farm planning and operation. In this study the performance of the two wind farms under two atmospheric conditions, a CNBL and a TNBL. While the TNBL assumes neutral conditions throughout the ABL and above, the CNBL represents a more complex and realistic modelling approach.

When the wind approaches a wind farm in a TNBL, the combined induction of the turbines creates a zone with increased pressure just before the start of the wind farm, redirecting the flow laterally and vertically. In a CNBL, the vertical component of the redirected wind interacts with a stable inversion layer aloft, which creates an enhanced high pressure area at the start of the wind farm, a phenomena commonly known as global blockage. At the end of the wind farm, the wind is directed down towards the low pressure region in the wake of the wind farm, lowering the inversion layer and creating a zone with even lower pressure. The combination of the two processes described, reduces the wind speed at the start of the wind farm and accelerates it towards the end.

In this study, we look at the interaction of two neighbouring wind farms at varying distances in both a TNBL and CNBL using the relatively fast Multi-Scale Coupled model (Stipa, Ajay, Allaerts, & Brinkerhoff, 2024) which uses a simplified mesoscale model to determine a background flow field which is then used to drive an engineering wake model. Each wind farm consists of a regularly aligned array of five turbines in the spanwise and ten turbines in the streamwise direction with a five rotor diameter (5D) spacing in both dimensions. The turbines are based on the 5 MW NREL reference (Jonkman et al., 2009) and simulations are run at a wind speed of 9 m/s at hub height, on the plateau of the thrust curve. For the CNBL simulations, we choose a Froude number of 1.0 for the inversion layer, resulting in maximum inversion layer displacement due to a phenomena called choking, and a Froude number of 0.10 for the free atmosphere.

Key findings (also summarised in Table 0.1):

1. For infinitely spaced wind farms in a CNBL, lower power output is seen compared to a TNBL due to stronger global blockage effects at the start of each wind farm despite a small speed-up towards the end of the farm.
2. For small wind farm separations (up to $\pm 72D$), the speed-up effect at the downstream end of the first wind farm enhances the power output of the second wind farm compared to a TNBL, whilst the blockage effect of the second wind farm negatively impacts the first wind farm.
3. The combined output of the two wind farms at small wind farm spacings is higher than when the farms are infinitely spaced, though lower than in a TNBL.

Table 0.1: Wind farm power output in a CNBL for an infinite wind farm spacing and a spacing of 25D, relative to a TNBL.

Wind farm	TNBL	CNBL infinitely spaced	CNBL 25D spacing
1	100%	98.1%	96.7%
2	100%	98.1%	101.8%
Total 1 and 2	100%	98.1%	99.3%

Contents

Preface	i
Abstract	ii
List of Figures	iv
List of Tables	v
List of Abbreviations	vi
1 Introduction	1
1.1 Context	1
1.2 State of the art	2
1.3 Problem description	3
1.4 Aims and objectives	3
1.5 Research questions	3
1.6 Structure of the report	4
2 Atmospheric boundary layer dynamics and wind farm interaction	5
2.1 Offshore atmospheric conditions	5
2.2 Wake recovery and atmospheric gravity waves	7
2.2.1 Cluster wake	7
2.2.2 Formation of the CNBL effects	7
2.2.3 Factors that affect the CNBL effects and atmospheric gravity waves	9
3 Methodology	11
3.1 Evaluation of CFD methods	11
3.2 Reduced-order model: MSC	12
4 Model setup	14
4.1 Model assumptions	14
4.2 Input	14
4.3 Wind turbine and farm layout	16
5 Results	18
5.1 TNBL versus CNBL velocity fields	18
5.1.1 Dominant inversion layer displacement effect	19
5.1.2 Lee wave effect	20
5.2 The effect of wind farm distance on the interaction	21
5.2.1 Effect of wind farm distance on the dominant inversion layer displacement effect	21
5.2.2 Effect of wind farm distance on the Lee wave effect	22
5.3 Prediction of the CNBL effect interaction	23
5.3.1 Interaction of the dominant inversion layer displacement effect	23
5.3.2 Interaction of the Lee wave effect	26
5.4 Power production	27
6 Conclusion	30
7 Discussion and recommendation	31
References	32
Appendices	36
Appendix A MSC output figures	36
Appendix B The effect of the Deeparray parameter	38
Appendix C MSC input	39
Appendix D Comparison between background velocity and streamwise velocity in TNBL and CNBL	41

List of Figures

1.1	Onshore and offshore wind power installations in the EU from 2024 to 2030	1
1.2	Turbine and cluster wake	1
1.3	Structure of the report	4
2.1	Atmospheric lapse rate and air parcel stability	5
2.2	Three-dimensional schematic representation of a CNBL	6
2.3	Effect of the Coriolis force on wind flow	7
2.4	An example of the pressure distribution in the ABL due to inversion layer displacement	8
2.5	An example of AGW interaction in the free atmosphere.	8
3.1	Turbulent energy spectrum	12
3.2	MSC iterative solution procedure	13
4.1	CNBL domain layout	15
4.2	Thrust and power coefficients	16
4.3	Wind farm and turbine layout.	17
5.1	Streamwise velocity profile for a wind farm distance 39.1D for TNBL and CNBL	18
5.2	The CNBL effects	19
5.3	The dominant inversion layer displacement effect	20
5.4	The Lee wave effect	21
5.5	The dominant inversion layer displacement effect as a function of wind farm distancing	22
5.6	The Lee wave effect for different wind farm distances	23
5.7	The dominant inversion layer displacement shown for two isolated, a combined and linear superimposed wind farm simulation	24
5.8	The dominant inversion layer displacement effect for a combined, linear superimposed and weighted superimposed wind farm simulation, for a wind farm distance of 123.3D	25
5.9	The dominant inversion layer displacement effect for a combined, linear superimposed and weighted superimposed wind farm simulation, for a wind farm distance of 39.1D	25
5.10	The Lee wave effect for a combined and linear superimposed wind farm simulation, for a wind farm distance of 39.1D	26
5.11	The Lee wave effect for a combined and linear superimposed wind farm simulation, for a wind farm distance of 9.7D	26
5.12	Row averaged velocity and power output for a wind farm distance of 39.1D	27
5.13	Power output per wind farm and combined for TNBL and CNBL as a function of wind farm distancing.	28
5.14	A comparison between the power output of a TNBL and CNBL simulation for WF1, WF2 and the total, as a function of wind farm distancing.	29
A.1	Streamwise perturbation velocity u_1 at hub height, normalised with the average velocity in the wind farm layer, for two offshore wind farms separated by 39.1D in a Conventionally Neutral Boundary Layer (CNBL)	36
A.2	Perturbation pressure p , normalised with the dynamic pressure, for two offshore wind farms separated by 39.1D in a CNBL	37
B.1	The effect of the Deeparray parameter on the difference in power output between a Truly Neutral Boundary Layer (TNBL) and CNBL simulation, for Upstream Wind Farm (WF1), Downstream Wind Farm (WF2) and the total of both wind farms. Also the isolated single wind farm simulations are visible with dashed lines.	38
D.1	Background velocity vs streamwise velocity difference TNBL and CNBL	41

List of Tables

0.1	Wind farm power output in a CNBL for an infinite wind farm spacing and a spacing of $25D$, relative to a TNBL.	ii
4.1	Parameters, formulas, values, and units for the wind farm simulations. For the parameters $\Delta\theta$ and Γ , the values for the TNBL and CNBL differ and is shown respectively.	15
4.2	Mesoscale domain parameters	16

List of Abbreviations

ABL	Atmospheric Boundary Layer
AGW	Atmospheric Gravity Wave
CA	CNBL Aligned
CFD	Computational Fluid Dynamics
CNBL	Conventionally Neutral Boundary Layer
CS	CNBL Staggered
DNS	Direct Numerical Simulations
EU	European Union
IBL	Internal Boundary Layer
LES	Large Eddy Simulation
MSC	Multi-Scale Coupled
pp	Percentage Point
RANS	Reynolds-averaged Navier-Stokes
RQ	Research Question
NREL	National Renewable Energy Laboratory
NS	Neutral Staggered
SAR	Synthetic Aperture Radar
TNBL	Truly Neutral Boundary Layer
TOSCA	Toolbox fOr Stratified Convective Atmospheres
WF1	Upstream Wind Farm
WF2	Downstream Wind Farm
3LM	3 Layer Model
3LMR	3 Layer Model Reconstruction

Nomenclature

$\Delta\theta$	Capping inversion strength [K]
ΔH	Capping inversion thickness [m]
η	Inversion layer displacement [m]
Γ	Free atmospheric lapse rate [K m ⁻¹]
κ	Von Kármán constant [-]
λ	Wavelength [m]
ρ	Air density [kg m ⁻³]
C_P	Power coefficient [-]
C_T	Thrust coefficient [-]
D	Rotor diameter [m]
f_c	Coriolis parameter [s]
Fr	Free atmospheric Froude number [-]
Fr_i	Inversion Froude number [-]
g	Gravitational acceleration [m s ⁻²]
g'	Reduced gravity [m s ⁻²]
H	Inversion layer height [m]
H_1	Wind farm layer height [m]
H_2	Upper layer height [m]
h_{hub}	Hub height [m]
L_f	Wind farm length [m]
N	Brunt-Väisälä frequency [s ⁻¹]
P	Power [W]
p	Pressure [Pa]
U	Streamwise wind velocity [m s ⁻¹]
u^{bk}	Depth-averaged background perturbation in x direction [m/s]
u_\star	Friction velocity [m s ⁻¹]
V	Lateral wind velocity [m s ⁻¹]
v^{bk}	Depth-averaged background perturbation in y direction [m/s]
x	Streamwise coordinate [m]
y	Lateral coordinate [m]
z	Height coordinate [m]
z_0	Surface roughness length [m]

1 Introduction

1.1 Context

In terms of size, quantity and installed capacity, wind farms are growing rapidly. The development of commercial wind turbines emerged in the 1970s, partly driven by oil limitations during the oil crisis (Office of energy efficiency & renewable energy, 2024). As the wind industry experienced rapid growth in the 21st century, turbines were grouped into wind farms to minimize installation, maintenance and grid connection costs. The rapid growth of wind power has continued to accelerate. From 2014 to 2023, the combined onshore and offshore wind power capacity in Europe doubled to 272 GW (Wind Europe, 2023), and it is estimated to reach 393 GW by 2030.

In the Netherlands the primary focus has shifted to offshore energy due to limited space on land. The offshore capacity growth between 2024 to 2030 is expected to expand from 4.6 GW to 15.6 GW (Wind Europe, 2023). During 2023, the Netherlands added 2.4 GW of wind energy, with offshore installations accounting for 78% of this new capacity. In Europe, wind energy currently supplies 19% of the electricity demand, with offshore wind contributing 21% to the total wind generation. Future plans are to greatly expand the offshore capacity of the European Union (EU), as shown in Figure 1.1.

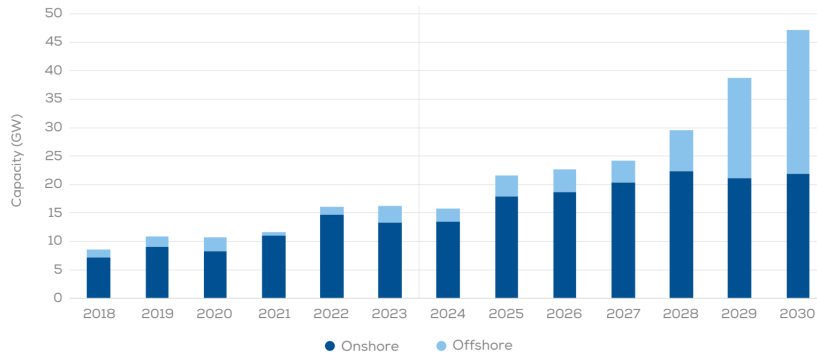


Figure 1.1: Onshore and offshore wind power installations from 2024 to 2030 in the EU (Wind Europe, 2023)

As offshore space becomes scarce, wind farms are positioned in closer proximity to one other. Therefore, this paper will cover the aerodynamic interaction between two neighbouring wind farms. Until now, most research has been performed on only the wake interaction between two offshore wind farms in a TNBL, which is a simplification of the actual temperature profile. Wake forms by the presence of the wind farm and its extraction of kinetic energy from the wind, which is converted to mechanical energy by the spinning of the blades, which in turn generates electricity. As a result, the mean wind flow behind the turbine decreases while turbulence increases. This is called wake for a turbine and cluster wake for a wind farm. A visualisation of the turbine and cluster wake is shown in Figure 1.2.



Figure 1.2: Turbine and cluster wake (Vattenfall, 2024)

As seen in Figure 1.2, the wake propagates far downstream. The extent of cluster wake propagation depends on

the atmospheric stability, turbulent intensity, boundary layer height, wind farm size, and layout (Schneemann et al., 2020; Cañadillas et al., 2020; Lanzilao & Meyers, 2022; Cao et al., 2023). For truly neutral conditions, the cluster wake can reach 30-35 km. This seriously affects the plans to build more offshore wind farms, because the wake could impact the energy production of a neighbouring wind farm significantly. Research by Nygaard and Hansen (2016) on the Nysted and Rødsand II wind farms revealed significant wake effects from the upstream wind farm on the downstream wind farm, particularly at the start of the second wind farm. Additionally, Cao et al. (2023) compared the power outputs of theoretical offshore wind farms at wind farm distances of 10D and 30D (D being the 126 m rotor diameter). Their findings showed that 30D spacing yielded 12.41% higher power output than 10D, highlighting the importance of inter-farm distance as a design parameter.

Next to wake effects, there are also second order effects that are important for offshore wind farms, especially by the increase in size of wind farms. Offshore atmospheric conditions are often characterized by a certain thermal stratification, one of which is the CNBL. The combination of the CNBL and the presence of the wind farm results in second-order effects referred to in this report as the "CNBL effects". Allaerts et al. (2018) has studied these CNBL effects and found that the power output is influenced in the order of 4-6%, calculated by using a relatively fast 3 Layer Model (3LM) on ERA5 data on the North Sea.

Furthermore, as the number of wind farms grows and the financial investments increase, understanding the interaction of clustered wind farms with the atmosphere becomes increasingly important. This will lead to higher profits and more efficient wind farm designs and support the sustainable development goals "Affordable and clean energy", "Sustainable cities", and "Communities and climate action" which should be reached by the end of 2030.

1.2 State of the art

Queney (1948) and Scorer (1949) were among the first to study lee waves, which are oscillations in the atmosphere triggered by the flow over mountains and returns to equilibrium, also referred to Atmospheric Gravity Waves (AGWs). Scorer (1949) gave the solutions for flow over a bell-shaped ridge by applying the linear theory. This research was followed by multiple theoretical and numerical studies on mountain waves (Gill, 1982; Durran, 1990; Inoue et al., 2014). Building on the work of Queney, Smith (1980) analysed three-dimensional mountain wave patterns, especially looking at the role of Froude number in whether the flow went around or over an isolated mountain. Following this, Long (1953), Durran and Klemp (1987), and Lott (1998) focused on AGWs as two-dimensional responses to two-dimensional topography, a concept expanded by Nastrom and Fritts (1992), who considered the effects of three-dimensional topographic perturbations. Accordingly, Smith (2010) created the two-layer model, which extends the linear hydrostatic 3D mountain wave theory by including a boundary layer bordering the free atmosphere. Later, this was enhanced again by Allaerts and Meyers (2019) to the three-layer model, which was able to capture the interaction between wind farm and gravity waves due to the addition of an extra layer. A recent advancement is the study of Stipa, Ajay, et al. (2024), who proposed the Multi-Scale Coupled (MSC) model, which uses 3LM to determine a background flow field which is then used to drive a micro-scale engineering wake model. Therefore, it captures local and global effects, including more advanced interactions between the wind farm and the atmosphere. More on this in Section 3.2.

Notable studies that investigated the effect of hills or mountains on wakes include Yang et al. (2015), which used Large Eddy Simulation (LES) to study how hill height affects the wake recovery in a TNBL. Ollier et al. (2018) studied the effect of a hill on a wind farm by comparing a control case without hill with a CNBL case with hill by using a $k-\epsilon$ turbulence model and lastly Draxl et al. (2020) looked at a real mountain and studied the variation of power output by the CNBL effects.

Studies that did research on self induced AGWs for large wind farms are Smith (2010); Abkar and Porté-Agel (2015, 2013, 2014); Allaerts and Meyers (2015, 2017); K. L. Wu and Porté-Agel (2017); Maas and Raasch (2022); Stipa et al. (2023); Lanzilao and Meyers (2023). They investigated how large farms may excite AGWs. The studies differed in several parameters: Atmospheric Boundary Layer (ABL) height which affects the AGWs and CNBL effects, model type, the layout and dimensions of the wind farm, and atmospheric conditions. A notable study from Allaerts et al. (2018) found based on hourly simulations of the year 2016 that the global blockage induced by the CNBL effects caused a deceleration of 0-5% in 75% of the simulations in the Belgian-Dutch offshore wind farm cluster. It was estimated that the annual energy loss due to the effect is 4 to 6%.

Then, there have been numerous studies that looked at farm-farm wake in a TNBL (Nygaard, 2014; Nygaard & Hansen, 2016; Veers et al., 2019; F. He et al., 2022; Cao et al., 2023; Baas et al., 2023; Hansen et al., 2015). They all conclude that installing a wind farm upstream can significantly affect the wind farm downstream. Furthermore, Van Der Laan et al. (2015) used a Computational Fluid Dynamics (CFD) - Reynolds-averaged

Navier-Stokes (RANS) model with a simplified $k - \epsilon$ model to simulate the turbulence in the ABL, to find the effect of the Coriolis force on the wake of a single wind turbine or wind farm. It was found that the effects on a single turbine are insignificant, but on a wind farm, the Coriolis force has a large impact. Paul Van Der Laan and Nørmark Sørensen (2017) also found that the wake curving is not because of local Coriolis force changes in the wake region, but due to existing wind veer in the atmosphere.

From these results, it is clear that self or topographically induced AGWs have been studied on individual wind farms. Furthermore, the wake effects in different atmospheric conditions between two neighbouring offshore wind farms have also been modelled and researched, as well as the CNBL effects on a single wind farm. Still, no study has yet determined what the CNBL effects are on two neighbouring offshore wind farms.

1.3 Problem description

As wind farms increase in size and number, the interaction between each other becomes more significant. The presence of the wind farm in a CNBL affects the flow field around the neighbouring wind farms, which has insufficiently been studied. This creates uncertainties in the predictions of energy production which could hinder wind farm expansion.

1.4 Aims and objectives

This study aims to increase the understanding of the aerodynamic interaction between two offshore neighbouring wind farms in a CNBL and how it affects the velocity fields within and around each wind farm. The objective is to improve our understanding of how the CNBL effects affect the power output of an offshore wind farm for different wind farm distancing. This research will contribute to the scientific community by enhancing our understanding of this topic, and eventually also governments and companies by supporting more effective planning of offshore wind farm clusters. These goals and objectives can be best achieved by answering a few critical Research Questions (RQs), which are given in the following section.

1.5 Research questions

1. How does a CNBL affect the flow field in the ABL and free atmosphere?
2. How is the flow field in a CNBL affected due to the interaction of two neighbouring offshore wind farms for different wind farm distances?
3. How is the power output in a CNBL affected for two neighbouring offshore wind farms for different wind farm distances?
4. What is the importance of simulating a CNBL instead of a TNBL, in relation to the regular wake effects for different wind farm distances?

1.6 Structure of the report

Section 2 gives a theoretical background on the ABL, focusing on its dynamics, thermal stability, and interactions with wind farms. Topics such as cluster wake recovery, local blockage, the inversion layer, the CNBL effects, and AGWs are covered. It answers RQ1. In Section 3, the methodology of this work is covered, which gives an introduction to CFD methods and more specifically the MSC model. The model setup is discussed in Section 4, which includes the model assumptions, input parameters, and the wind turbine and wind farm layout. Section 5 contains the results of the performance of single and multiple wind farms under CNBL, including wake dynamics and energy production. It answers RQ2, RQ3 and RQ4. Finally, the last sections are the conclusion, and discussion and recommendations in Section 6 and Section 7, respectively. An overview of the report is shown in Figure 1.3.

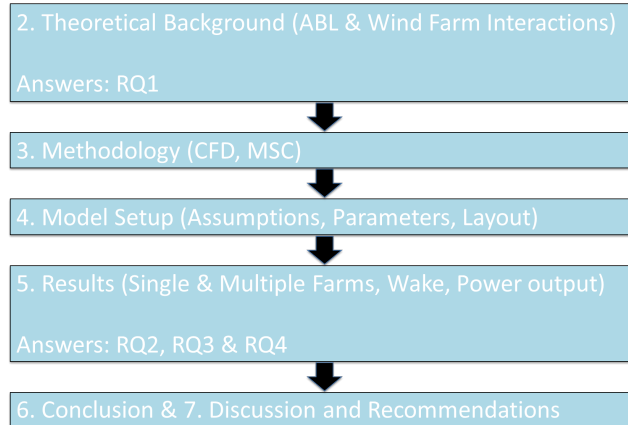


Figure 1.3: Structure of the report

2 Atmospheric boundary layer dynamics and wind farm interaction

This chapter provides the fundamental theoretical background, needed to understand the complex interactions between offshore wind farms, and with the atmosphere. Key characteristics of the offshore environment include atmospheric conditions, stability types, the CNBL, and the Coriolis force. Then this chapter will cover wake recovery mechanisms, the CNBL effects, and AGWs. Lastly, it will be explained how the flow field affects the wind farm differently for other atmospheric and wind farm parameters.

2.1 Offshore atmospheric conditions

In the absence of a heating force at the surface, no wind, and no other convection forces, density stratification occurs. Dense air descends, and less dense air ascends due to gravitational effects, which results in a stable layer. An alternative way of reasoning is that hot air rises and cold air sinks, which results in a temperature gradient, also known as lapse rate. Yet atmospheric absolute temperature decreases with elevation. The key is that potential temperature should be regarded when defining a stable layer. Potential temperature is defined as: *"the temperature an air parcel would have if it were expanded or compressed adiabatically from its existing pressure to a pressure of 1000 mbar or 100 hPa"* (Nappo, 2012). Adiabatic means that the air parcel can only change in temperature due to compression or expansion and no heat is exchanged with its environment. As an air parcel rises, it expands due to the decreasing surrounding atmospheric pressure, resulting in a temperature decrease. Another key concept that one should know to understand the stability of offshore atmospheric conditions is the environmental lapse rate, which is the temperature gradient of the atmosphere with altitude. To conclude, when an air parcel is moved upward, both the temperature of the atmosphere and the temperature of the air parcel with altitude change. The relation between the environmental and adiabatic lapse rates will determine the stability of the air parcel.

For example, the dry adiabatic lapse rate is typically $9.8\text{ }^{\circ}\text{C}/\text{km}$, while the environmental lapse rate is highly variable but approximately $6.5\text{ }^{\circ}\text{C}/\text{km}$ (Talley et al., 2011; Dutra et al., 2020). These rates are illustrated against the altitude z in Figure 2.1a. When forcing an air parcel upward, as shown in Figure 2.1b, it cools faster than the surrounding atmosphere. As it becomes relatively heavier, it will sink back to its original altitude. However, if the environmental lapse rate is larger than the dry adiabatic lapse rate, the exact opposite behaviour is expected. An upward motion will lead to a further upward motion. This is an unstable atmosphere. When both lapse rates are equal, the atmosphere is neutral.

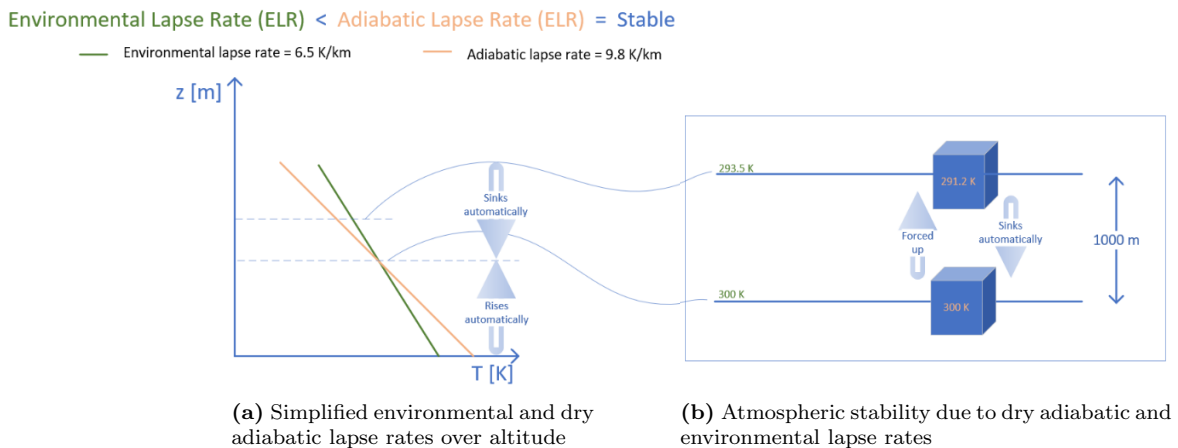


Figure 2.1: Atmospheric lapse rate and air parcel stability

Offshore conditions are characterised by long wind fetches with low surface roughness. This causes, together with the constant temperature of the sea due to the high heat capacity, a constant flow of wind. As the air layer interacts with the sea surface, it gradually takes on the temperature of the sea up to a certain equilibrium height. This forms an inner layer, called an Internal Boundary Layer (IBL), and forms due to sudden changes in temperature or roughness. It is often referred to as the height where the ratio of the time-averaged velocity and the inflow velocity at the same height, taken in a plane 2 km upwind, reaches a value of 97% (Allaerts & Meyers, 2017; Y. T. Wu & Porté-Agel, 2013). The complete inner layer now has the same potential temperature

and is referred to as a TNBL. The atmosphere above this IBL is unaffected, and thus, a sudden jump in temperature profile is needed to make equilibrium with the higher altitudes. The layer where the sudden jump in temperature is located is called the inversion layer or capping inversion and is, therefore, very stable. The neutral layer beneath the inversion layer is the ABL, and the stable layer above the inversion layer is the free atmosphere. This temperature profile is called the CNBL and is schematised in Figure 2.2.

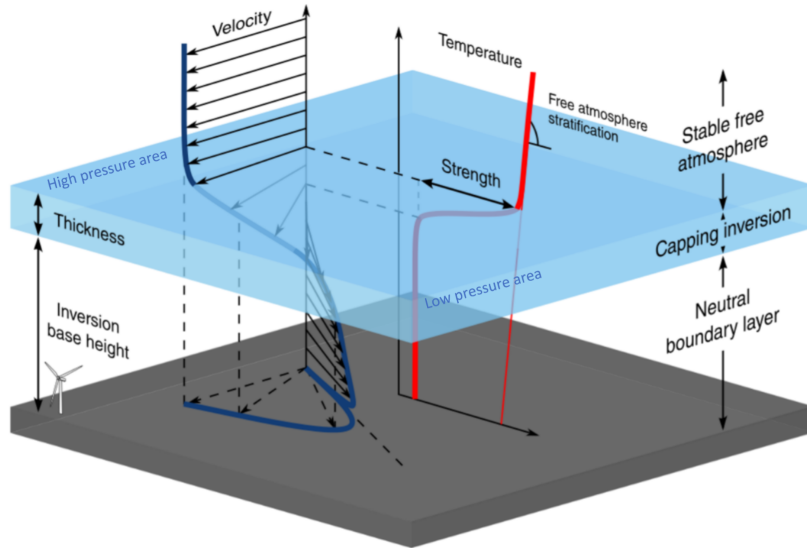


Figure 2.2: Schematic representation of a CNBL. Modified version of Allaerts and Meyers (2015). The velocity temperature profile over altitude is shown, where the inversion layer strength is defined by the temperature jump in the inversion layer.

The stability of the inversion layer acts as a barrier to turbulent mixing and vertical movements. Its strength is determined by the temperature jump and thickness and determines how much of the processes in the ABL are passed through to the free atmosphere. The start of the inversion layer for offshore conditions is typically between 200 to 700 m and has a thickness of around 100 m (Brost et al., 1982; Grant, 1986; Tjernstrom & Smedman, 1993).

Another process visible in Figure 2.2, is the Coriolis force, which exists due to the rotation of the earth. This force redirects the wind flow towards the right in the northern hemisphere and the left in the southern hemisphere. In a non-rotating world, wind flows from high to low pressure, but realistically, the Coriolis force affects the flow until an equilibrium has been reached between the pressure gradient and the Coriolis force. This process is shown in Figure 2.3. One can see how V_1 is the original direction of the wind speed but is affected by the Coriolis force C_1 , which is always perpendicular to the wind direction. Consequently, V_2 is affected again by the Coriolis force C_2 until an equilibrium is reached, the geostrophic wind. The strength of the Coriolis force and how fast the equilibrium is reached depend on factors like the velocity of the wind, altitude, and mass. The Coriolis force is an important factor that should be taken into account when looking at wind flow between wind farms because it changes the wind direction and reduces the growth of the ABL (Van Der Laan et al., 2015; Zilitinkevich et al., 2007).

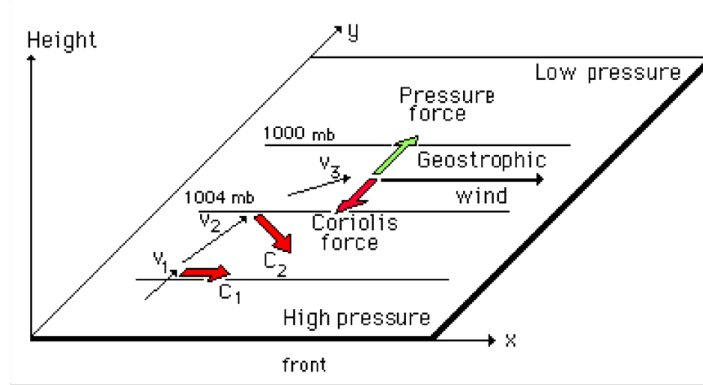


Figure 2.3: Effect of the Coriolis force on wind flow in the northern hemisphere (Sorbjan, 2003). V_1 , V_2 , and V_3 illustrate the evolution of wind direction over time, which also affects the direction of the Coriolis force directly. Also the straight isobars are visualized.

2.2 Wake recovery and atmospheric gravity waves

2.2.1 Cluster wake

A wind turbine disturbs the wind flow as it decreases the mean flow speed and increases the turbulence behind the wind turbine, which is called wake. In a wind farm, the interaction of the wake of multiple wind turbines results in complex wake patterns called cluster wake. The development and formation of cluster wake depend on multiple factors, like turbine spacing, atmospheric stability, wind velocity, and the size of wind turbines or farms. These cluster wakes create large disturbances that extend far downstream, especially due to the fact that the surface roughness is very low above the sea. Analytical and numerical flow models have predicted the far wake up to 100 km in stable conditions, while Synthetic Aperture Radar (SAR) data have shown effects as far as 55 km (Hasager et al., 2015; Platis et al., 2018) downstream.

Furthermore, the interaction of different wakes and the surrounding air is an important aspect of cluster wake because it shows how the cluster wake recovers, which is important for the second wind farm, regarded in this research. Allaerts and Meyers (2017) looked at a wide wind farm with 20 rows of turbines with a streamwise spacing of $7.5D$. This results in a wind farm length of 15 km and a width of 4.8 km, which covers the complete width of the domain. By looking at the energy budget analysis, it is clear that the energy extracted by the wind turbines comes from flow deceleration and vertical turbulent entrainment. Vertical turbulent entrainment refers to the mixing of faster-moving air above and around the wind farm with the slower-moving air within the wind farm. This causes the wind to recover too in and after the wind farm. It is shown that the vertical turbulent entrainment is small at the beginning but becomes dominant near the end of the wind farm and reaches a steady value after eight turbine rows.

2.2.2 Formation of the CNBL effects

Due to the presence of an offshore wind farm and the extraction of wind energy, the wind is slowed down. The slower wind interacts with the faster wind from upstream, causing it to change direction away from this local higher pressure zone. This is called local blockage and has negative effects on the power output of the wind farm due to a decrease in the mean wind speed. The local blockage pushes the wind around the wind farm and upwards. The vertical upward component displaces the inversion layer upwards. This extra space must be filled with surrounding potential cold air, adding extra weight to the entire air column underneath. This causes a higher pressure in front and at the start of the wind farm, slowing the wind. This is called global blockage and is noticed further upstream than local blockage, an effect of the presence of the inversion layer. Then, at the end of the wind farm, little wind comes out, resulting in a local low-pressure area. The wind that flows over the wind farm, will therefore fall, resulting in a downward component, which pulls the inversion layer down with it. This results in a smaller air column and, thus, a second-order low-pressure area. As a result, the wind is slowed down at the start of the wind farm, but further in the wind farm, pushed and pulled through the wind farm due to the pressure gradient. This displacement of the inversion layer enhances the wake recovery (Allaerts & Meyers, 2017; Y. T. Wu & Porté-Agel, 2013; Smith, 2010). The pressure induced is generally assumed linearly dependent on the vertical displacement of the inversion layer as described by Equation (1).

$$\frac{p_1}{\rho_0} = g' \eta_t \quad (1)$$

where η_t is the inversion layer displacement, ρ_0 the reference density and p_1 the pressure at the displaced layer, and g' is the reduced gravity defined in Equation (2):

$$g' = g \frac{\Delta\theta}{\theta_0} \quad (2)$$

in which $\Delta\theta$ the potential temperature difference across the inversion layer and θ_0 the reference potential temperature.

An example from Lanzilao and Meyers (2023) of the increase in pressure at the start and decrease at the end of the wind farm is shown in Figure 2.4, where the inversion layer height is 500 meters. Furthermore, a 2D top view of the pressure distribution in this paper for a certain configuration of wind farms can be found in Appendix A.

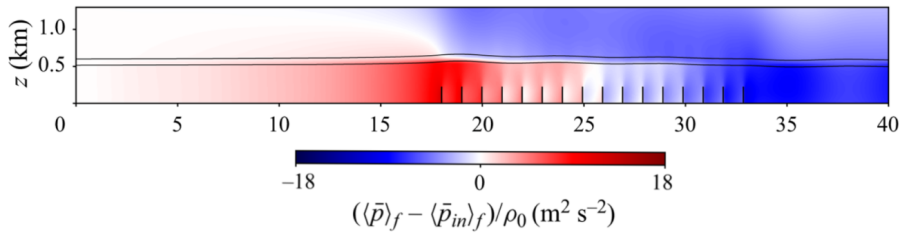


Figure 2.4: An example of the pressure distribution in the ABL due to inversion layer displacement (Lanzilao & Meyers, 2023)

Secondly, the displacement of the inversion layer at the start and end of the inversion layer causes also waves in the free atmosphere, called AGWs. The AGWs at the start and end of the wind farm interact with each other and do affect the flow field in the ABL via affecting inversion layer displacement. An example of visualisation is given in Figure 2.5, where vertical velocity is plotted on a vertical slice at different simulation intervals.

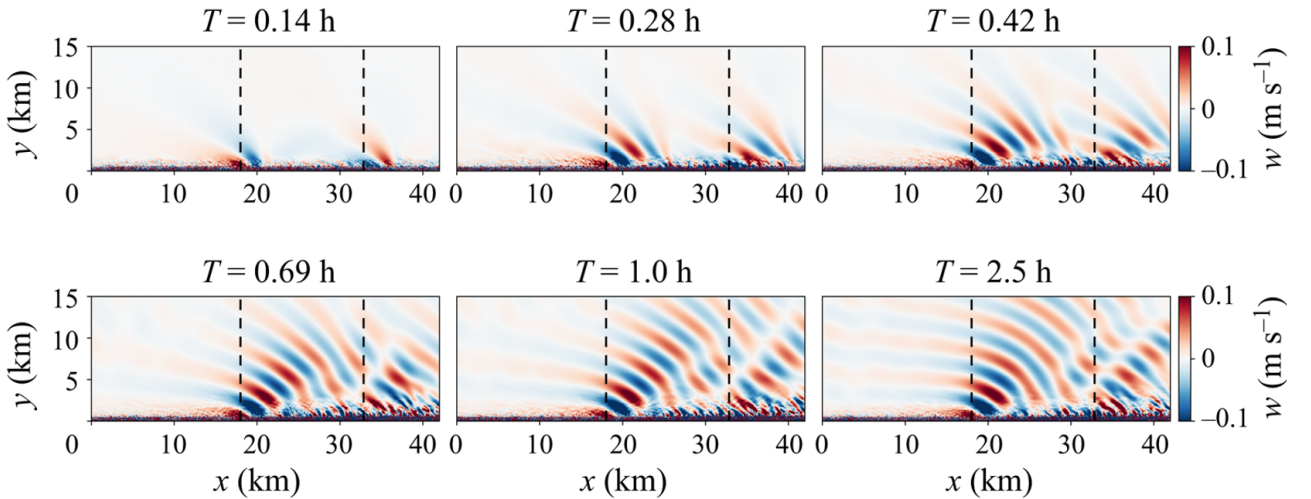


Figure 2.5: An example of AGW interaction in the free atmosphere over time (Lanzilao & Meyers, 2023), where y represents altitude and w vertical velocity.

As mentioned earlier, Allaerts et al. (2018) showed how a CNBL affects the power output of the Belgian-Dutch offshore wind farm cluster. They found by performing hourly simulations of the year 2016 that the global blockage induced by the inversion layer displacement caused a deceleration of 0-5% of the free-stream velocity in 75% of the simulations. Under certain atmospheric conditions, the deceleration became even more than 10%. Annually, the energy loss due to self-induced gravity waves is estimated to be 4-6%. There are certain

conditions where the power output could increase because the effect of the favourable pressure gradient is larger than the unfavourable pressure gradient (Lanzilao & Meyers, 2022). This raises the question of what influences the CNBL effects and thus the power output, which will be discussed in Section 2.2.3.

2.2.3 Factors that affect the CNBL effects and atmospheric gravity waves

The appearance of the pressure distribution in Figure 2.4 and AGW interaction in Figure 2.5, is highly dependent on wind turbine layout, windfarm layout, height of the inversion layer and Froude number in both the inversion layer and free atmosphere. The Froude number that describes the AGWs along and atop the inversion layer, also named interfacial AGWs is defined by Equation (3) as:

$$Fr_i = \frac{U_g}{\sqrt{g'H_i}} \quad (3)$$

in which U_g the geostrophic wind, H_i the height of the midpoint of the inversion layer and g' the reduced gravity as described in Equation (2). Furthermore, the Froude number, which describes the AGWs in the free atmosphere, often referred to as internal AGWs is defined in Equation (4),

$$Fr = \frac{U_g}{NL_f} \quad (4)$$

where L defines the length of the wind farm and the Brunt-Väisälä frequency N is defined by Equation (5) as:

$$N = \sqrt{\frac{g}{\theta}\Gamma} \quad (5)$$

where Γ defines the lapse rate in the free atmosphere given as $\frac{d\theta}{dz}$.

Allaerts and Meyers (2019) has an extensive study done on how the Fr_i affects the CNBL effects. The key points are that when Fr_i increases above 1, the interfacial waves cannot travel upwind, and thus, the inversion layer is displaced further downstream. Consequently, the higher pressure falls within the wind farm, leading to a lower power output. Also the positive pressure gradient causes less of a recovery compared to a subcritical case. Lastly, it is also important to note that power output is sensitive to the strength of the inversion layer as shown by Allaerts (2016), but the boundary layer height appears to be more important.

The following studies have researched what effect the height of the inversion layer, the layout of the wind farm, the atmospheric stability, the strength of the inversion layer, and the wind farm width-length ratio have on the power output. These will all be discussed below.

The height of the ABL

Allaerts and Meyers (2017) researched 3 different inversion heights; 1000 m, 500 m and 250 m. It was found that lowering the boundary layer height from 1000 m to 500 or 250 m caused a rise, in displacement of the inversion layer from 75 to 97 m. Accordingly, the pressure in the ABL caused by the inversion layer displacement is also higher for a lower inversion height. Wind flows more difficult over the wind farm which limits turbulent energy transport and causes more global blockage. Also, the 1000 m case has its maximum pressure at the beginning of the wind farm, which is favourable for the wind speed in the wind farm. For the other cases (lower inversion height), the maximum pressure is located further downstream in the wind farm, which is unfavourable. Decreasing the inversion height from 1000 to 250 m, results in a power loss of around 6 to 9 Percentage Point (pp). The main reason for this is the decrease of turbulent energy transport having a decrease of 12 pp, which is the wake recovery due to the layers above and around the wind farm that speed up the wind in the wind farm. Next to the decrease of turbulent energy transport, the mechanical energy divergence decreases with only 5 pp, which is a combination of mean flow energy fluxes and pressure gradients.

Allaerts (2016), also looked at how changing the boundary layer height affects the wind farm for the same atmospheric conditions except for the inversion layer height. It was found that comparing an inversion layer height of 500 m to 1000 and 1500 m resulted in an energy increase of $(25 \pm 0.3)\%$ and $(31 \pm 0.4)\%$, respectively.

Layout and atmospheric stability

Lanzilao and Meyers (2022) has studied how a CNBL Staggered (CS) vs a CNBL Aligned (CA) layout in a finite wind farm have different effects on the wind farm efficiency. Furthermore, Lanzilao and Meyers (2022)

looked also at how the CNBL effects, affect the wind farm efficiency by comparing a Neutral Staggered (NS) wind farm with a CS. By using LES, it was concluded that the gravity wave increased the wind farm efficiency for the CS by 8.8% even though the blockage was also largest for CS compared to CS and NS. This is due to the fact that the larger blockage effect also caused a more favourable pressure gradient, which enhances the wake recovery significantly. Lastly, the CS case resulted in a lower wake recovery than in NS. This, in combination with a higher blockage, results in NS having an efficiency that is 4.5% higher than CS.

Strength of the inversion layer

Allaerts (2016) performed a study covering many aspects. One of the aspects that was thoroughly studied was how changing the strength of the inversion layer from 2.5 to 10 K/km had an effect on the wind farm output. The initial thickness of the inversion layer is 100 m. Allaerts found by using LES on a very large wind farm of 180 turbines over a fetch of 15 km, that a higher inversion strength (thus 10 K/km) results in a (13 +- 0.2)% lower power output.

Abkar and Porté-Agel (2013) also used LES to study the influence of the free atmosphere lapse rate by looking at a lapse rate of 1 to 10 K/km. No capping inversion layer is defined in this study. The power output decreases by 35% when going from 1 to 10 K/km. Due to the high inversion strength, less vertical energy transport can be transferred from the free atmosphere to the ABL, resulting in lower power production.

Wind farm width-length ratio

Allaerts and Meyers (2019) performed a study to see how different parameters have an effect on the CNBL effects. It was found that the effects are small for wind farms that are very long or wide because wind can flow easily around them. Its maximum is at a width/depth ratio of around 3/2 because this configuration causes the most disturbances to the flow, leading to larger self-induced induced pressure fields, which in turn influence the wind farm.

3 Methodology

The methodology chapter gives the overall framework used to simulate wind farm performance by choosing a method that balances computational time and accuracy. This approach covers the use of CFD methods for both high-fidelity, low-fidelity, and reduced-order models. In particular, the MSC model is highlighted for its effective coupling of the turbine scale wake effects with the mesoscale effects, giving a practical alternative to LES.

3.1 Evaluation of CFD methods

Different methods are available to simulate how wind behaves in a domain. CFD methods, which solve fluid flow equations numerically, and analytical engineering models, which use simplified mathematical formulas. These methods vary significantly in their computational requirements and accuracy, which will be discussed in this subsection.

CFD models could be categorised into different parts, dependent on what part of the eddy scale it solves. The largest scale is the energy-producing range, the eddies that interact with the mean flow and extract energy from it. Then, on the intermediate scale, called the inertial sub-range, they receive energy from the large eddies and pass it down to the smaller ones on the smallest scale, the dissipation range. Here, the eddies convert the energy into heat. See Figure 3.1 for a typical turbulent energy spectrum.

The high-fidelity methods are Direct Numerical Simulations (DNS) and LES. DNS solves the complete Navier-Stokes equations without any turbulence modelling, resulting in the most accurate solution. This method is extremely computationally expensive and not practical for wind farm simulations. Then, a commonly used CFD method is LES, which is more practical by only solving the large-scale eddies in the energy-containing range and inertial sub-range and modelling the small eddies using a subgrid-scale model in the dissipation range. Toolbox for Stratified Convective Atmospheres (TOSCA) is an example of an open-source LES model and is designed for wind farm simulations. Low fidelity CFD models include RANS model, which splits the flow into a mean and fluctuating component. Then, it only solves for the mean flow in the energy-containing range, which contains most of the energy, while modelling all turbulent fluctuations. Some widely used RANS models are Prandtl's and k-epsilon models. Please see Figure 3.1 for the part of the energy spectrum that is typically solved and modelled for DNS, LES, and RANS.

Engineering models use assumptions to achieve very fast computation times. The Jensen model is a simple, analytical wake engineering model with one adjustable parameter, the wake decay coefficient (Kollwitz et al., 2016) for example, and is used for a quick initial design.

Between CFD and engineering models are reduced-order models like 3LM, which simplify the physics while retaining key phenomena. The 3LM divides the atmospheric boundary layer into 3 layers and solves the depth-averaged Navier-Stokes equation to capture wind farm-atmosphere interactions. The model applies some degree of coupling, but the coupling between the turbine-scale wake effects and the mesoscale global effects is weak (Stipa, Ajay, et al., 2024). Then another model is MSC, which captures both local (turbine-scale) and global (wind farm-scale) effects. Unlike 3LM, which over-predicts velocity deficits and struggles with blockage effects, MSC uses the fast 3LM to determine a background flow field, which is then used to drive an engineering wake model, allowing it to better account for the pressure gradients and thermal stratification. This leads to more accurate power predictions, only 2% underestimation compared to LES, while 3LM overestimates power production, especially in supercritical conditions. A disadvantage of the reduced-order models is that they only show the steady state and not the transient phase or the vertical wind profile.

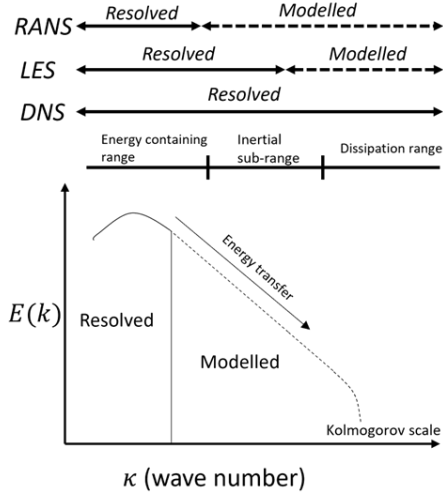


Figure 3.1: Turbulent energy spectrum, where turbulent kinetic energy $E(k)$ is plotted against the wave number k , which is the inverse of the eddy size.

The MSC model is used in this study due to its efficiency and accuracy (verbal permission obtained from authors and The University of British Columbia Okanagan Computational Fluid Dynamics Laboratory). An introduction to this model is given below.

3.2 Reduced-order model: MSC

The reduced-order MSC model (Stipa, Ajay, et al., 2024) is made to couple the effects between large wind farms and the atmosphere. It considers both the micro-scale effects, such as turbine wake and wind turbine induction, and mesoscale effects, such as atmospheric gravity waves and farm-scale interactions. The model combines the micro and mesoscale components by assuming that the effects occur at separate spatial scales and can be linearly superimposed. It also assumes incompressible flow. MSC thus uses a linearised, depth-averaged Navier-Stokes equations for the wind farm layer and the upper layer of the ABL. For each layer, these equations include momentum conservation in horizontal directions x and y , mass conservation, turbulent diffusion, terms accounting for Coriolis force, a momentum exchange between the two layers, and a wind farm forcing term representing the filtered turbine thrust forces.

The steps to solve this model are summarised in Figure 3.2. In the initialisation step, a uniform inflow velocity is given at micro-scale level together with initial thrust coefficients C_T , which are used to calculate turbine thrust. Ground effects are included by a method where the turbines are mirrored to the ground. Notably, this mirroring is only used in the MSC model, not other reduced-order models. There is also an option to use a log-profile velocity inflow.

Then, for the mesoscale steps, the turbine thrust forces are smoothed out on the 3LM grid using a Gaussian filter. The 3LM equations, which model vertically-averaged values in each layer, are solved in Fourier space, which means that the undamped perturbations will be recycled after entering the domain. The 3LM then solves for u_1, v_1, u_2, v_2 , inversion layer displacement η , and perturbation pressure p . Subscript 1 refers to the wind farm layer, which is defined as twice the hub height. Subscript 2 is the rest of the ABL. u and v are the velocities in the horizontal x and y directions.

In the next step named 3 Layer Model Reconstruction (3LMR), the perturbation pressure from the 3LM solution is used as a forcing term, but without the presence of the wind farm. With this, the depth-averaged background perturbation velocity is determined, named u^{bk} and v^{bk} in the paper of Stipa, Ajay, et al. (2024). In the MSC code, this is referred to as ur_1 and ur_2 , where r refers to reconstructed for layers 1 and 2, respectively. This only contains the large-scale pressure effects. Then, using the approach of Panofsky, this is transformed to a height-dependent velocity profile, dependent on the friction velocity, equivalent roughness length, and the von Karman κ constant. The reconstruction matches the magnitude of the local background velocity profile $U_b(x)$ with the layer average $U_1 + u_1^{bk}$ in the wind farm layer. It assumes variations due to large-scale pressure gradients only affect the friction velocity while preserving the logarithmic profile shape. In the paper, this reconstructed height-dependent velocity field is called $U_b(x)$. However, in the actual code implementation, the

height-dependent $U_b(x)$ is calculated for a certain amount of points and stored in the variable u^{bk} . Each turbine is represented by 16 quadrature points arranged in a cross pattern for improved resolution of partial waking and vertical gradients.

The micro-scale calculation interpolates the reconstructed height-dependent velocity at hub height to the quadrature points for the micro-scale model. Then, this is combined with the wake effects and local blockage effects using linear superposition of analytical models: the Bastankhah wake model and the Vortex Cylinder model, respectively. For local blockage, turbine self-induction is not considered to prevent taking into account the same effect twice since thrust coefficients from turbine power curves already include self-induction effects. The micro-scale velocities are denoted as u in the code and $U(x)$ in the paper.

The iteration process updates C_T and C_P coefficients, which are dependent on the new velocity and continues until the pressure residual calculated using the L2 norm falls below a specified tolerance, typically requiring 4-5 iterations for a 10^{-4} tolerance, or the specified amount of iterations has been reached. For this study, the iterations process stops after three iterations because it has been shown by Stipa, Ajay, et al. (2024) that the power distributions for this amount are within 0.5% of the power distribution of 5 iterations.

While the MSC model offers significant computational advantages over high-fidelity simulations, it has some limitations. It provides reduced fidelity compared to LES, only steady-state solutions, and requires periodic lateral boundary conditions due to its Fourier-based solver. However, the MSC model underestimates power output by approximately 2% compared to LES, which is a significant improvement over other reduced-order models.

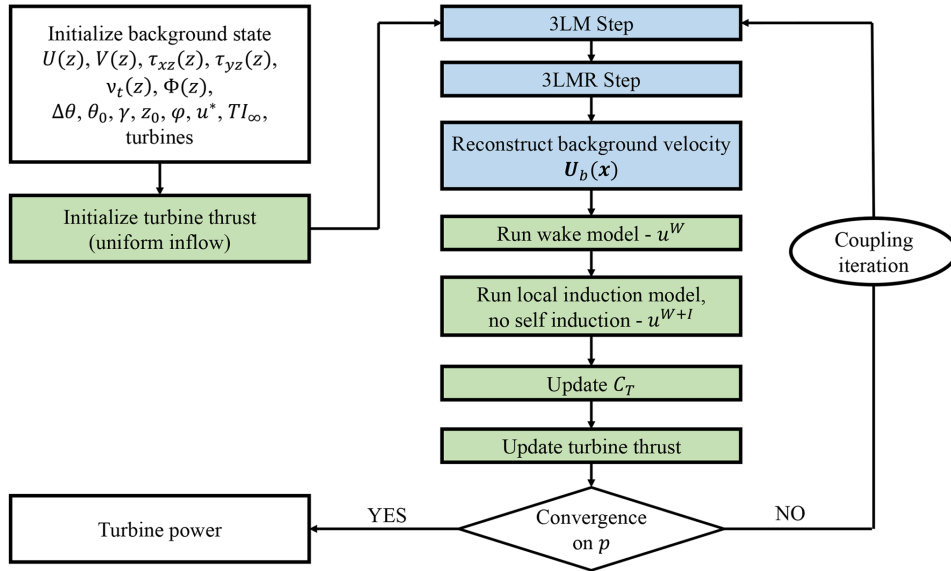


Figure 3.2: MSC iterative solution procedure (Stipa, Ajay, et al., 2024). Green defines the micro-scale model, and blue the mesoscale model.

4 Model setup

This chapter presents the model setup and key assumptions used to study the interaction between the wind farms, using the MSC model. Also, a tabular and visual overview of the used turbine, parameters, turbine spacing, and domain characteristics is given in this chapter.

4.1 Model assumptions

This study looks at the farm-farm interaction and while MSC could visualise the micro-scale effects, the output files are 8 GB per simulation, which obstructs the purpose of the use of this model. It also increases the computational time significantly, from approximately 12 minutes to 40 minutes for a single simulation.

Furthermore, the deep-array effect is turned off for the same reason as aforementioned. It increases the computational time even up to 2 hours. Furthermore, the results showed small differences. A comparison of the absolute difference between the TNBL power output and CNBL power output of Figure 5.13 has been made in Appendix B with and without deep-array on.

Furthermore, MSC has some built-in assumptions. The micro-scale and mesoscale effects are linearly superimposed. Furthermore, incompressible flow is assumed, which is an assumption that is probably not true for the 5 MW National Renewable Energy Laboratory (NREL) wind turbine. The rated rotor speed is 12.1 rpm (Feliciano et al., 2018), which transfers to 80 m/s at the tip of the turbine blade. At this velocity, it is expected that the air behaves compressible. For this study, the far wake effects are observed and it is assumed that the local effects of the blade are small. Furthermore, Maas (2023) has researched the effects of this assumption and concluded that this approach works very well for studying wind farm wake.

4.2 Input

To investigate the CNBL effects, the choice has been made to investigate a realistic parameter space, which causes maximum inversion layer displacement. It has been assumed that the Coriolis force is 0. The wind speed is an important parameter and is chosen to be close to the average calculated wind speed between 2016 and 2022 at the North Sea at turbine height, 9 m/s (TNO, 2023). Furthermore, the surface roughness is 0.1 mm, which is a value related to a calm sea (Lanzilao & Meyers, 2023), the inversion layer strength is 4.95 K, the lapse rate in the free atmosphere is 7.7 K/km for the CNBL simulation, and a reference temperature of 300 K. For the TNBL simulation the inversion layer strength and lapse rate are both set to 0. Please see Table 4.1 for all values and formulas used, and a visualisation in Figure 4.1. For a more extended version of the input parameters in MSC, please see Appendix C. To see all realistic ranges of the parameter on the North Sea, please look at the research of Lanzilao and Meyers. This is the case for an inversion layer Froude number of 1 when a phenomenon called choking takes place. The information at critical Froude number will not travel upstream, but remain fixed in position, causing an extra high pressure. It is important to note that MSC uses the Nieuwstadt model, which is a model that evaluates the depth-averaged velocities for the different layers in the atmosphere. While the initial parameters are specified to get a certain Froude number, the actual value could deviate slightly.

Parameter	Symbol	Formula	Value	Unit
Froude number	Fr	$U_g/(NL_f)$	0.10	–
Inversion layer Froude number	Fr_i	$U_g/\sqrt{g'H_i}$	1.00	–
Reduced gravity	g'	$g\Delta\theta/\theta_0$	0.16	m/s^2
Distance between turbines	S_x	$5D$	630	m
Brunt-Vaisala frequency	N	$\sqrt{g\Gamma/\theta_0}$	0.016	s^{-1}
Length of the wind farm	L_f	$9 \times 5D$	5.67	km
Width of the wind farm	L_w	$4 \times 5D$	2.52	km
Inversion layer height	H_i	–	500	m
Model inflow wind velocity	U_{ref}	–	9.0	m/s
Inversion layer strength	$\Delta\theta$	–	0.0 or 4.95	K m
Reference temperature	θ_0	–	300	K
Gravitational acceleration	g	–	9.81	m/s^2
Rotor diameter	D	–	126	m
Hub height	h_{hub}	–	90	m
Lapse rate (Free atmosphere)	Γ	$d\theta/dz$	0.0 or 7.7	K/km
Surface roughness	z_0	–	0.0001	m
Initial thrust coefficient	C_T	–	0.85	–

Table 4.1: Parameters, formulas, values, and units for the wind farm simulations. For the parameters $\Delta\theta$ and Γ , the values for the TNBL and CNBL differ and is shown respectively.

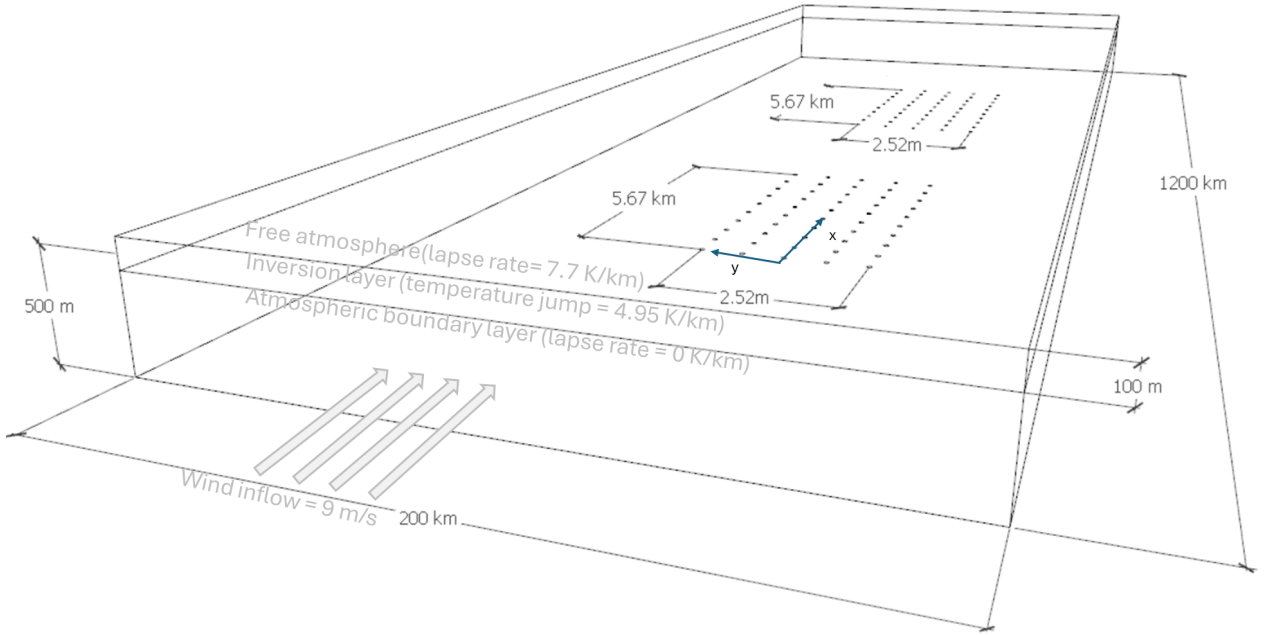


Figure 4.1: CNBL domain layout (not to scale).

As explained in Section 3.2, the thrust and power coefficients are dependent on wind speed and are updated every iteration. Unfortunately, these are not publicly available; thus, in MSC, the coefficients, shown in Figure 4.2, are acquired from various previously ran LES simulations.

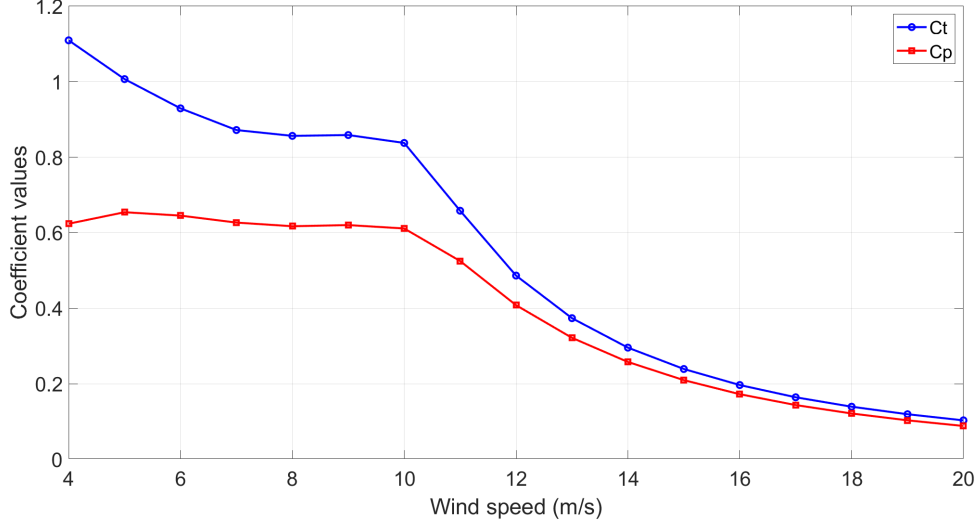


Figure 4.2: Thrust and power coefficients acquired from LES solutions of the NREL 5MW turbine.

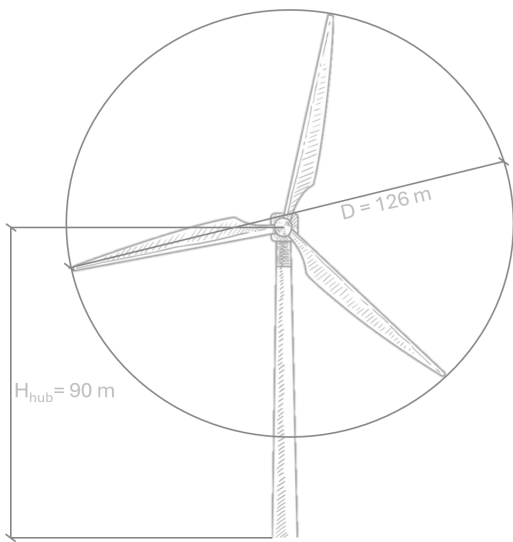
4.3 Wind turbine and farm layout

To run the simulations, the NREL 5 MW reference wind turbine, which has extensively been used in wind turbine and farm analysis, will be used. Even though current wind farms like Borssele have larger turbines, around 9 MW (Rijksoverheid, 2021), the NREL 5 MW is used to be able to compare the results to other studies. Also, its dimensions and most parameters are publicly available. Its hub height is 90 m and its diameter is 126 m. The values are shown in Figure 4.3a.

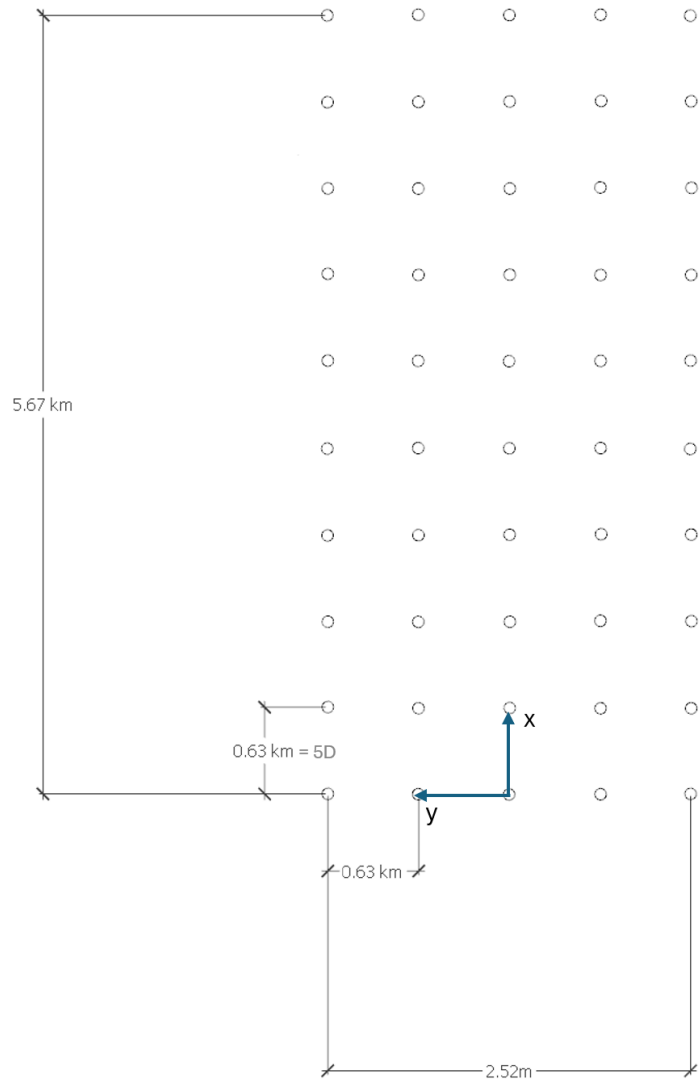
Name	Symbol	Value	Unit
x mesoscale domain start	$x_{s,meso}$	-200	km
x mesoscale domain end	$x_{e,meso}$	1200	km
y mesoscale domain start	$y_{s,meso}$	-100	km
y mesoscale domain end	$y_{e,meso}$	100	km
x direction discretization	dx_{meso}	250	m
y direction discretization	dy_{meso}	250	m

Table 4.2: Mesoscale domain parameters

The turbine spacing of the theoretical wind farm is 630 meters or 5D in crosswind and streamwise direction, which is within the limits of recommended wind turbine spacing and also used in other studies (Gupta, 2016; Stipa, Khan, Allaerts, & Brinkerhoff, 2024). Furthermore, the wind farm has 10 rows and 5 columns as shown in Figure 4.3b, which is an average size of a wind farm in the U.S. (USGS, 2022). For the domain sizes, a very large domain is used due to the fact that MSC uses periodic boundary conditions as aforementioned in Section 3.2. By increasing the domain length up to 1400 km, the effects were minimal. Furthermore, the width of 200 km appeared to be sufficient to make sure no waves recycle back in the domain and enter the second wind farm. For the mesoscale, which captures the large-scale effects, a discretization size of 250 meters is chosen instead of the 500 meters used in (Stipa, Ajay, et al., 2024).



(a) 5-MW NREL wind turbine layout with a hub height of 90 m and a rotor diameter of 126 m



(b) Wind farm layout for both wind farms

Figure 4.3: Wind farm and turbine layout.

5 Results

This chapter presents a comparison of the solution of a wind farm simulation in a TNBL and a CNBL to investigate the CNBL effects, which are categorised as: the dominant inversion layer displacement effect and the Lee wave effect. MSC has been used and generated output files, of which a selected amount are presented in Appendix A. The first effect occurs due to the initial and dominant inversion layer displacement, creating a high pressure at the start and a low pressure at the end. The latter effect refers to the oscillating waves in the inversion layer from this displacement. First, the velocity field comparison between the TNBL and CNBL is presented, followed by an analysis of how these effects change with wind farm distancing. Finally, the power output will be analysed and explained by relations found in the velocity analysis. One could have done the same analysis for the inversion layer displacement or pressure, as they show similar relations. When the inversion layer increases, the pressure increases, and the velocity decreases. This analysis uses velocity as it is easiest to comprehend and directly used to calculate power.

5.1 TNBL versus CNBL velocity fields

The comparison of a TNBL and CNBL simulation begins by examining the streamwise velocity u_1 along the middle column of the wind farms at hub height. This velocity profile is shown in Figure 5.1. The free-stream velocity is 9 m/s, and the wind farms are separated by 39.1D. The wind farm rows are visualised by vertical lines. Only the range between 40 km upstream and 80 km downstream of WF1 is shown to be able to compare the simulations. The wake effect, which is defined by the negative deviation from 9 m/s, becomes less when going even further downstream; at 600 km, $u_1 = 8.8$ m/s, and at 1200 km, $u_1 = 8.97$ m/s.

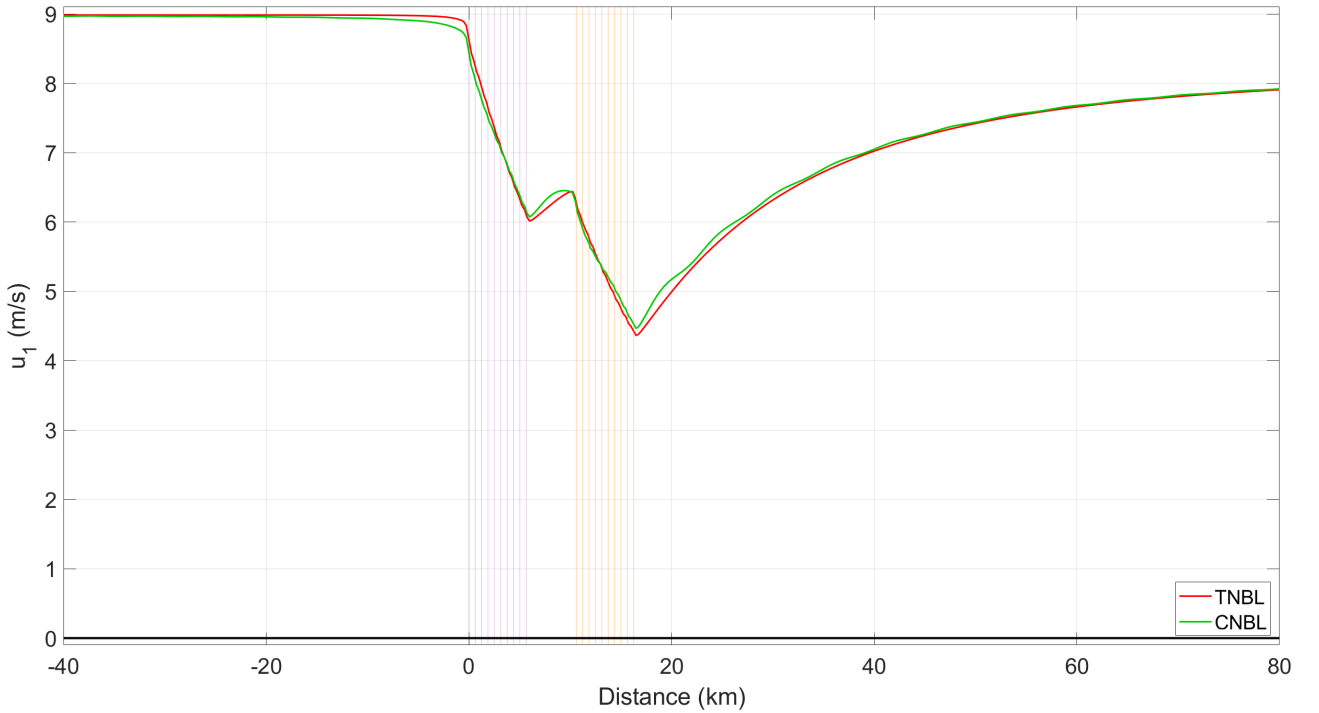


Figure 5.1: Streamwise velocity profile u_1 in the wind farm layer for a wind farm distance 39.1D for TNBL and CNBL. The wind farm rows are visible as vertical lines.

By comparing the graphs, one can see that before WF1 and at the beginning of the WF1, the velocity profile of the CNBL simulation is below the TNBL simulation due to the global blockage effect. At the end and downstream of WF1, the velocity profile of CNBL is higher than the TNBL simulation, which is due to the pressure gradient that speeds up the flow in CNBL. The same relation can be found for WF2, but one can already see that the CNBL graphs exceed the TNBL graph further upstream in the wind farm compared to WF1, which shows that possibly some interaction takes place. This is not certain because the inflow velocity differs for WF2. By subtracting the two graphs, one can find the difference between the CNBL and TNBL simulation, thus CNBL effects. This is shown in Figure 5.2. It is important to note that another method to analyse the CNBL effects, is to consider the background velocity u^{bk} . This method takes into account that the

flow is confined under a rigid lid, the displacement of the inversion layer and the initial flow. Subtracting the velocity profiles which has been done in this study, neglects the last term. Also the development of the flow develops slightly differently in both methods. A comparison between the velocity profile of the two methods has been made in Appendix D, which shows small differences between the velocity profiles

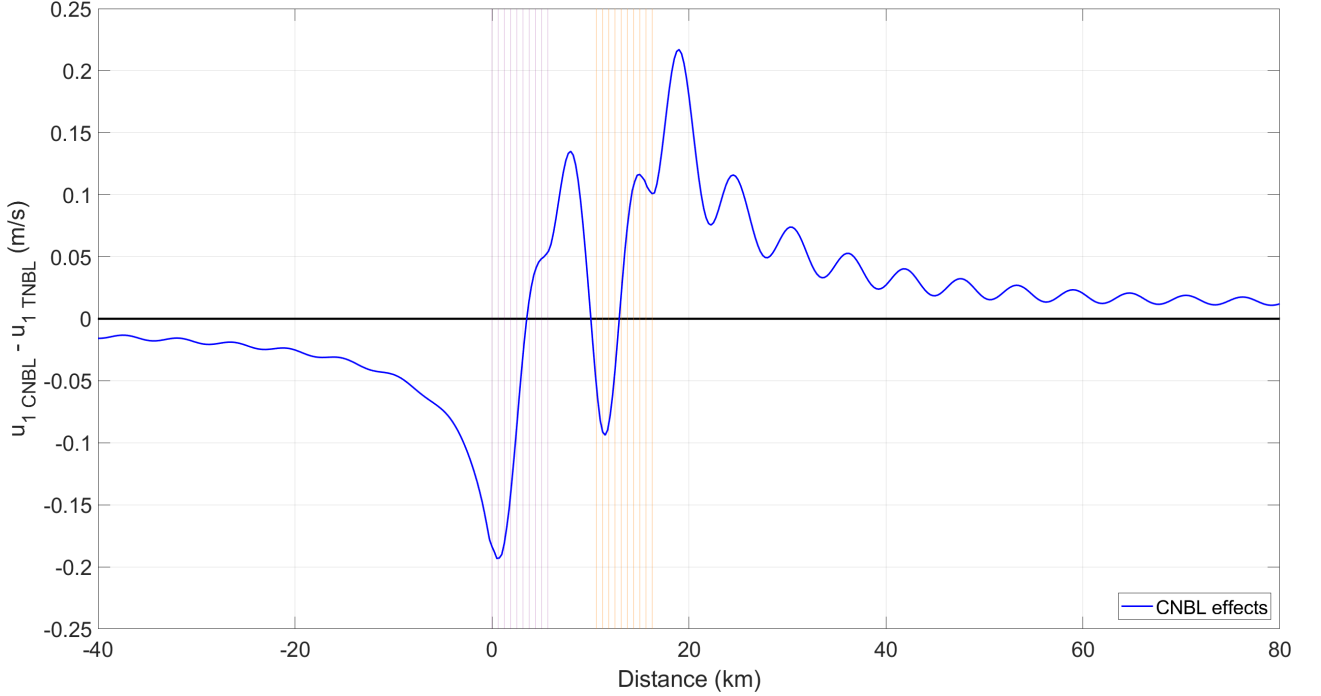


Figure 5.2: The CNBL effects for a wind farm distance of 39.1D. The wind farm rows are visible as vertical lines

When the velocity profile is negative, it means that at that location, the CNBL simulation experiences more of the global blockage than the speed-up effect, compared to the TNBL simulation. This means a local slowdown due to the CNBL effect. When the graph is positive, it indicates that the CNBL effects enhance the local wind speed relative to the TNBL case, referred to as a speed-up.

One can see that the global blockage effect in WF1 is larger than in WF2, and the speed-up in WF2 is larger than in WF1. This is because the CNBL effects of a wind farm extend beyond its boundaries and start to interact with similar effects caused by the other wind farm.

To analyse the CNBL effects, the harmonic perturbation caused by the displacement of the inversion layer, which is the Lee wave propagating via the inversion layer, should be separated from the dominant displacement perturbation. This will result in two different CNBL effects: "the dominant inversion layer displacement effect" and "the Lee wave effect." In the next subsections, these two CNBL effects will be analysed.

5.1.1 Dominant inversion layer displacement effect

To isolate the dominant inversion layer displacement effect, the moving average is taken from Figure 5.2 with a window of 5.65 km, which is the downstream wavelength shown in Figure 5.2. Note that this wavelength is not entirely constant in Figure 5.2 due to the interaction of WF1 and WF2. The dominant inversion layer displacement effect is shown in Figure 5.3.

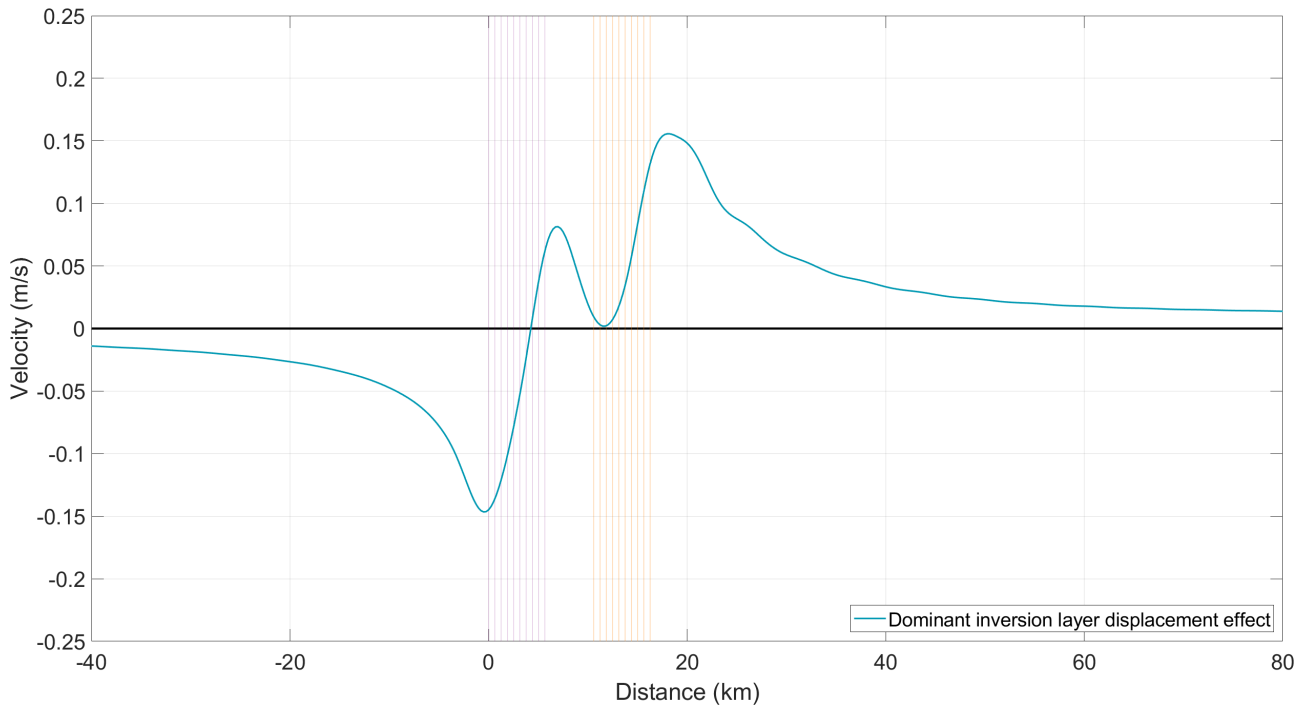


Figure 5.3: The inversion layer effect at a wind farm distance of 39.1D. The wind farm rows are visible as vertical lines.

Again, positive values indicate that the CNBL effects enhance the local wind speed relative to the TNBL simulation, and negative values indicate a reduction of local wind speed. One could see that the global blockage effect starts to increase faster, approximately 30 km upstream of WF1. Within WF1 the graph becomes positive after turbine 8, while the graph stays positive during all of WF2. The reason for this is that WF2 experiences the speed-up of WF1, creating a higher local velocity compared to the TNBL simulation.

5.1.2 Lee wave effect

To isolate the Lee wave effect, the dominant inversion layer displacement effect (Figure 5.3) is subtracted from the CNBL effects (Figure 5.2). This removes the moving average component, isolating the Lee wave effect as shown in Figure 5.4.

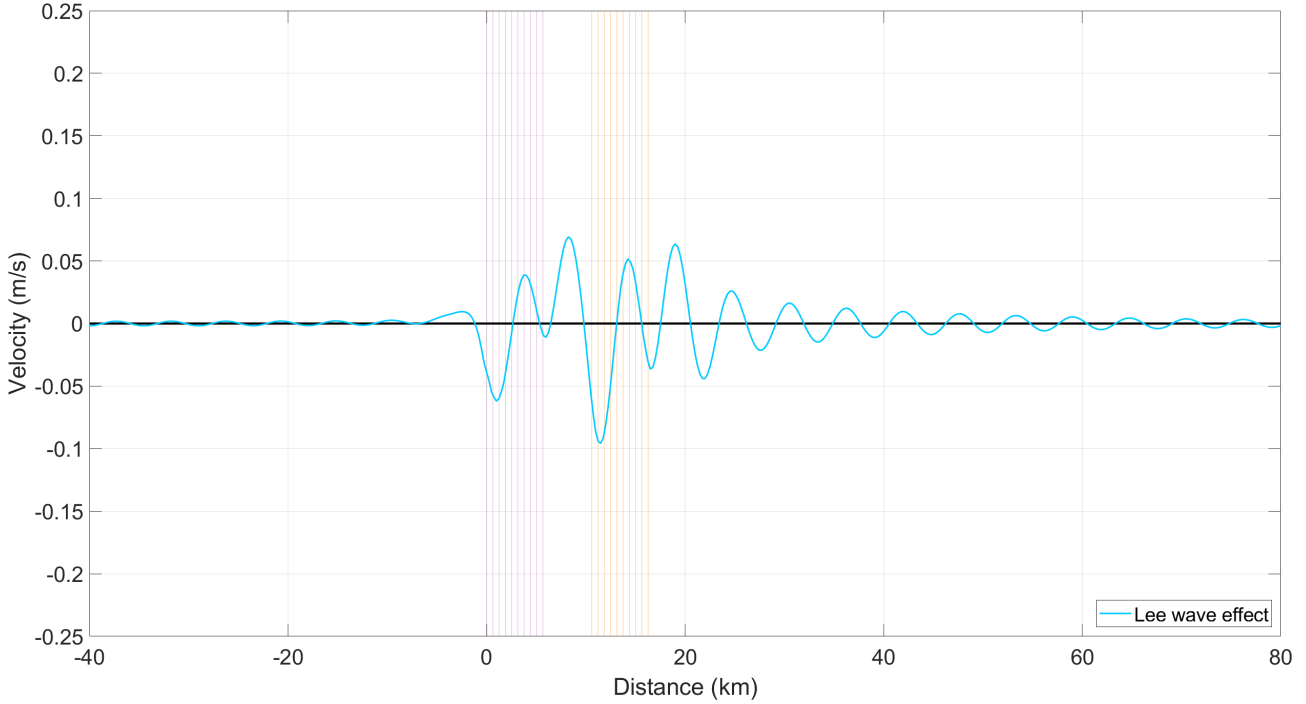


Figure 5.4: The Lee wave effect at a wind farm distance of $39.1D$. The wind farm rows are visible as vertical lines.

It is observed that the upstream effects are very small in front of WF1, indicating that WF2 has little influence on WF1. Furthermore, one does see large effects downstream of WF2, indicating that WF1 has relatively large effects on WF2. This idea is supported by comparing the first trough in WF1 with the first trough in WF2. The trough in WF2 is way larger; thus it is expected that the Lee waves from WF1 resonate with the inversion layer displacement caused by WF2, which will be verified in Section 5.2.2.

5.2 The effect of wind farm distance on the interaction

The interaction between WF1 and WF2 is expected to depend highly on the distance between the WFs and is therefore investigated in this subsection. First, the effect of distance on the dominant inversion layer displacement effect, and then the effect of distance on the Lee wave effect is presented.

5.2.1 Effect of wind farm distance on the dominant inversion layer displacement effect

The dominant inversion layer displacement effect is shown in Figure 5.5, from an infinitely distanced wind farm up until a wind farm distance of $5.4D$, which is almost equal to turbine distancing $5D$. The wind farm distances beyond $98.0D$ are omitted from this part of the analysis to maintain figure clarity, except for the infinitely distanced wind farm. The infinitely distanced wind farm is simulated by placing a single isolated wind farm in the domain.

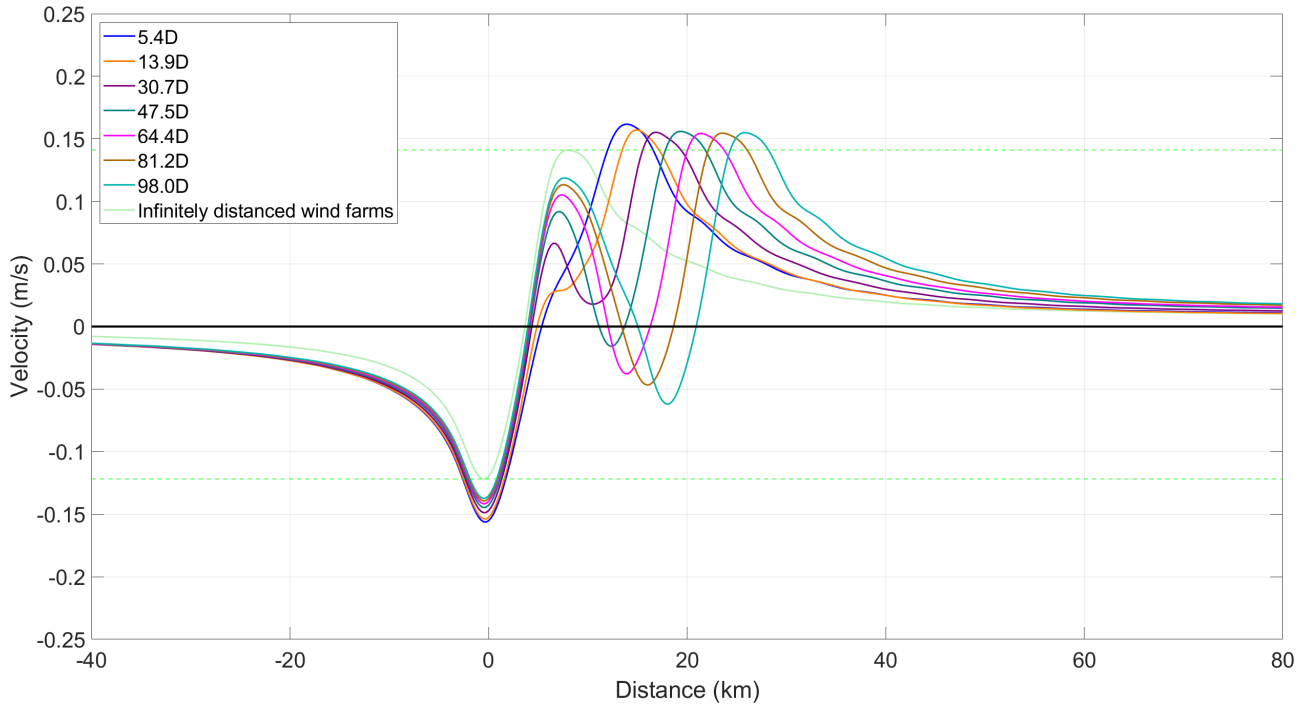


Figure 5.5: The dominant inversion layer displacement effect as a function of wind farm distancing. For the infinitely distanced wind farms, its minimum and maximum is emphasised with a horizontal dashed line

Looking at the velocity profile of infinitely distanced wind farms, one can see the dominant inversion layer displacement for an isolated wind farm. Note that for this simulation, the velocity plot is unique; it shows the lowest amount of the global blockage effect and the highest wake recovery due to the strongest favourable pressure gradients for WF1 among the simulated wind farm distances.

As wind farm distance decreases, significant interactions occur between the speed-up of WF1 and the global blockage of WF2, from the start of WF1 until the end of WF2. Especially the speed-up of WF1 and the global blockage of WF2 interact. The speed-up of WF1 enhances the velocity in WF2, and the global blockage of WF2 decreases the velocity in WF1. Still, it appears that the speed-up of WF1 is stronger than the global blockage of WF2. For example, the graph for 30.7D stays far above zero velocity. Whether this will positively affect the power production will follow from the power analysis in Section 5.4.

5.2.2 Effect of wind farm distance on the Lee wave effect

For the Lee wave effect, different wind farm distances are plotted, ranging from 9.7D until infinitely distanced wind farms, shown in Figure 5.6. Note that the y-axis range has been adjusted to be able to compare the plots.

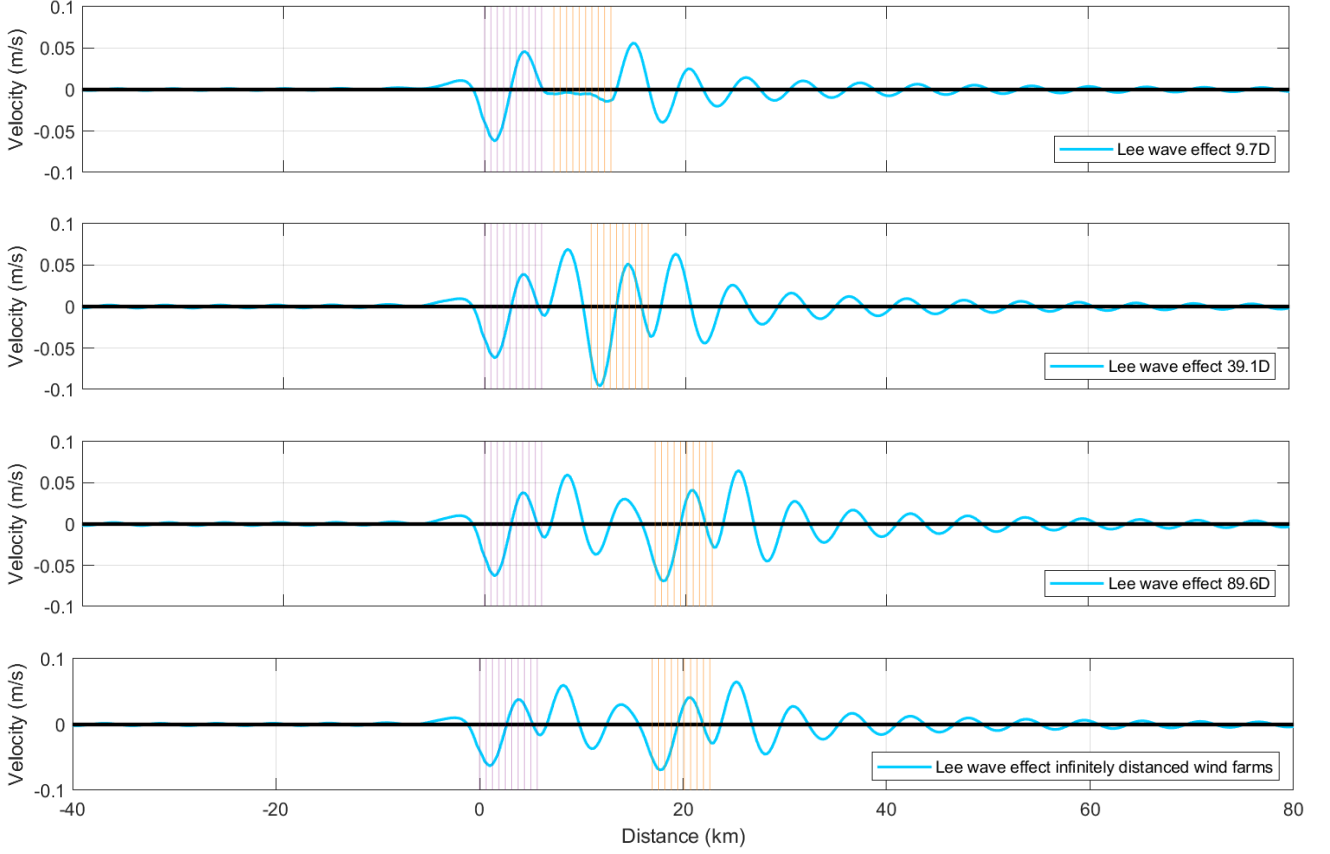


Figure 5.6: The Lee wave effect for different wind farm distances. The wind farm rows are visible as vertical lines.

By looking at the velocity profile of the infinitely distanced wind farm, one can see that the Lee wave effects are significantly smaller than the dominant inversion layer displacement effect. Furthermore, the upstream effects are very small compared to the downstream effects as mentioned in Section 5.1. Therefore, as wind farm distance decreases, the velocity profile of WF1 does not change significantly, while within WF2, constructive and destructive interactions are visible for a wind farm distance of 9.7D and 39.1D, respectively. Beyond 89.6D, the interaction between the wind farms is very small for the Lee wave effect. Lastly, the wavelength of the Lee wave effect has approximately the same length as the wind farm for this parameter space.

5.3 Prediction of the CNBL effect interaction

To get a better understanding of how the wind farms interact, a relation needs to be found on how both the wind farms contribute to their combined CNBL effect velocity profile. The combined CNBL effect can be obtained by superimposing the individual CNBL effects of two isolated wind farms after applying scaling factors dependent on distance to account for their contributions as given in Equation (6). To get the effect of a single isolated wind farm, a simulation is run for WF1 and WF2 each.

$$\text{Combined CNBL effect} = \text{factor}_1(x) \cdot \text{isolated CNBL effect WF1} + \text{factor}_2(x) \cdot \text{isolated CNBL effect WF2} \quad (6)$$

Again, this relation will be sought for the dominant inversion layer displacement effect and the Lee wave effect.

5.3.1 Interaction of the dominant inversion layer displacement effect

in Figure 5.7, the dominant inversion layer displacement effect is plotted for three simulations: an isolated WF1, an isolated WF2, and a combined simulation of both. Next to this, the linear summation of the individual isolated wind farms is plotted in red without the usage of factor_1 and factor_2 .

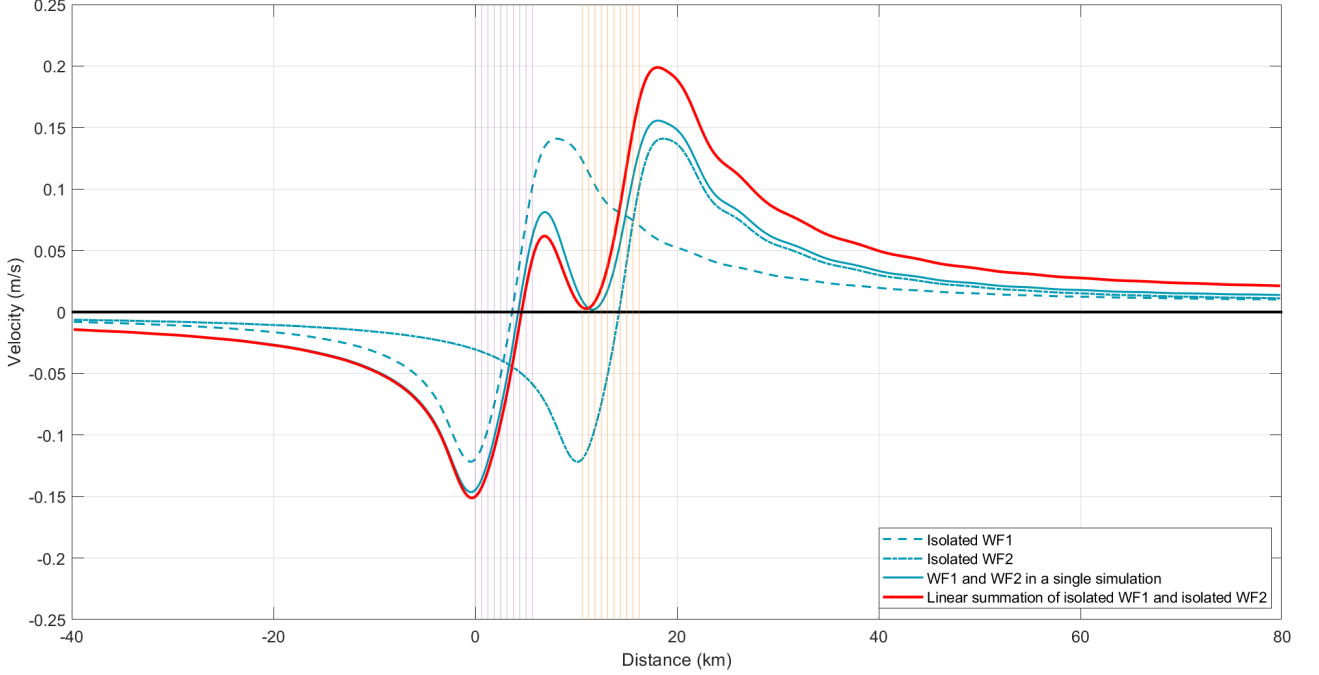


Figure 5.7: The dominant inversion layer displacement effect for an individually isolated and combined wind farm simulations, for a wind farm distance of 39.1D. Also the linear summation of the single isolated wind farm simulations is shown. The wind farm rows are visible as vertical lines.

As expected, there is no linear relation. But it is visible that before and within WF1, the combined simulation closely follows the line of the single simulation of WF1. And also the other way around within and downstream of WF2. This gives the idea the isolated WF1 is a good estimation of the combined effect of WF1 and WF2 in a single simulation. The same counts for WF2, downstream of WF2. This means that $factor_1 = 1$ could be a good estimate upstream of WF1, and $factor_2 = 1$ a good estimate downstream of WF2.

An interesting point is that before WF1, the distance between the "Isolated WF1" graph and the "WF1 and WF2 in a single simulation" graph is larger than the distance downstream of WF2 between the "Isolated WF2" and the "WF1 and WF2 in a single simulation" graphs. This gives the idea that WF2 affects the velocity upstream of WF1, more than WF1 affects the velocity downstream of WF2. This is unexpected as the downstream speed-up effects are larger than the global blockage effects as shown for the single wind farm simulation in Figure 5.5, but can be explained by the non-linear relation. It does mean that $factor_2$ needs to be larger upstream of WF1 than $factor_1$ downstream of WF2.

Furthermore, in Figure 5.5, the dominant inversion layer displacement effect between WF1 and WF2 shows stronger positive values than would be expected from a linear superposition of individual wind farm effects, suggesting an exponential or power-law relationship.

With these points in mind, the relation given by Equation (7), Equation (8) and Equation (9) is found and fitted for a good match.

$$factor1(x) = factor1_{after_WF2} + (factor1_{before_WF1} - factor1_{after_WF2}) \cdot decay(x) \quad (7)$$

$$factor2(x) = factor2_{after_WF2} + (factor2_{before_WF1} - factor2_{after_WF2}) \cdot decay(x) \quad (8)$$

$$decay(x) = 1 - \left(\frac{x - WF1_{start}}{WF2_{end} - WF1_{start}} \right)^{2.5} \quad (9)$$

The factors shown in Figure 5.8 show a good fit for relatively large wind farm distancing, i.e., 123.3D.

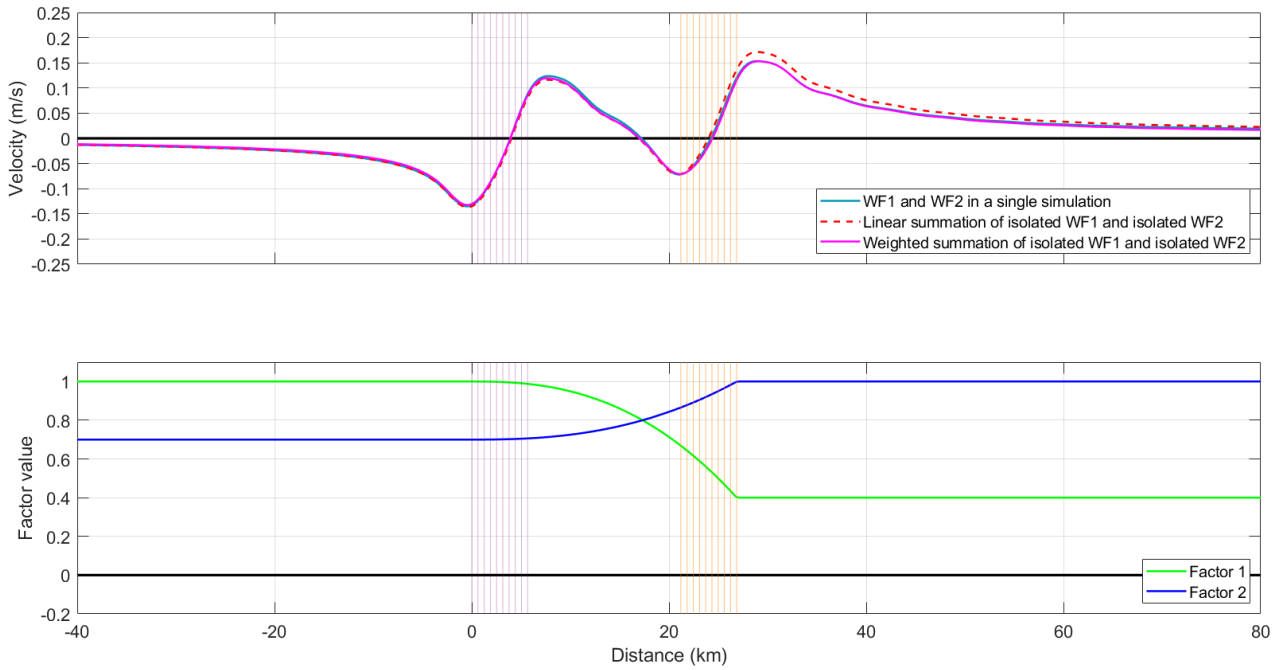


Figure 5.8: The dominant inversion layer displacement effect for the linear superposition of the single isolated wind farm simulation, the weighted superimposed and the combined wind farm simulations, for a wind farm distance of 123.3D. $factor_1$ and $factor_2$ are shown in the lower figure, which are used for the weighted summation. The wind farm rows are visible as vertical lines.

However, when the wind farm distance is decreased, the fit becomes less accurate. To improve the fit, the magnitude of the effects of WF2 need to be damped more and more. An example of a smaller distance with a smaller $factor_2 = 1$ is shown in Figure 5.9, for a wind farm distance of 39.1D.

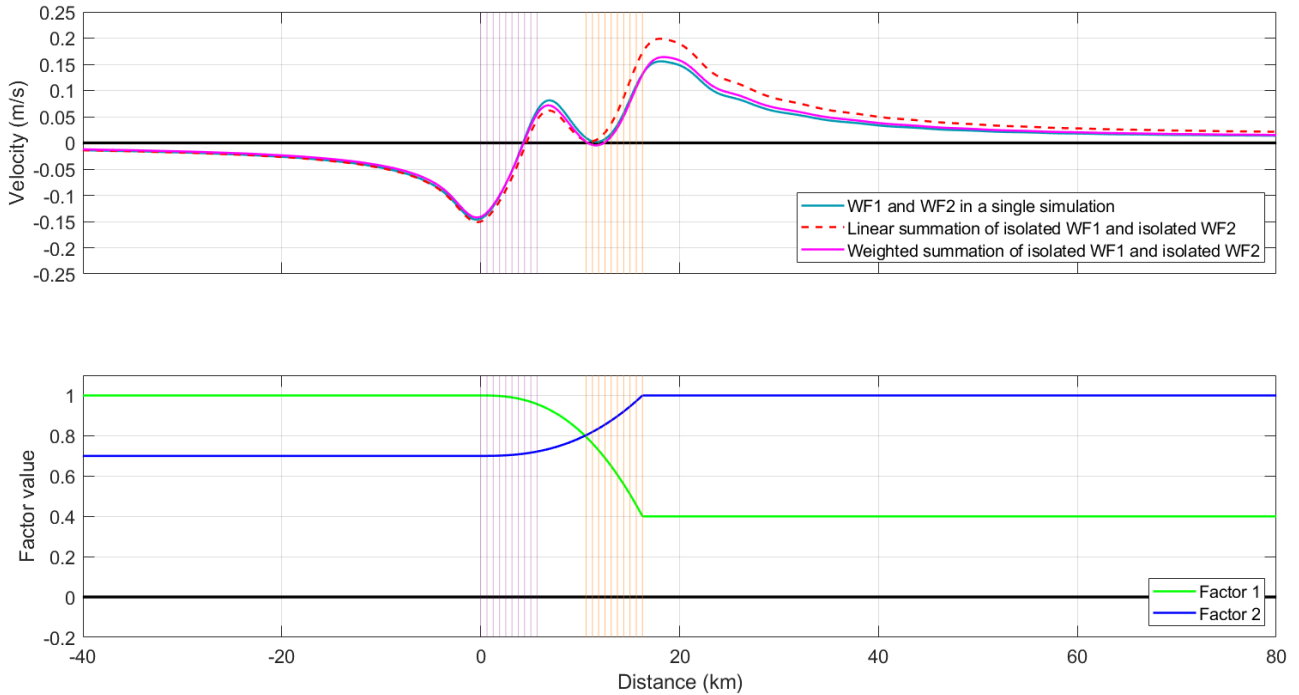


Figure 5.9: The dominant inversion layer displacement effect for the linear superposition of the single isolated wind farm simulation, the weighted superimposed and the combined wind farm simulations, for a wind farm distance of 39.1D. $factor_1$ and $factor_2$ are shown in the lower figure, which are used for the weighted summation. The wind farm rows are visible as vertical lines.

As wind farm distancing varies, WF2 experiences different inflow conditions due to varying upstream velocities and because the flow is redirected by WF1. These different flow conditions reduce the inversion layer displacement due to WF2, leading to a lower $factor_2$ value.

5.3.2 Interaction of the Lee wave effect

The same analysis is performed for the Lee wave effect. Thus, a simulation of both wind farms in a simulation and a linear summation of both isolated wind farms is shown in Figure 5.10, for a wind farm distance of 39.1D. Surprisingly, the linear summation works pretty well.

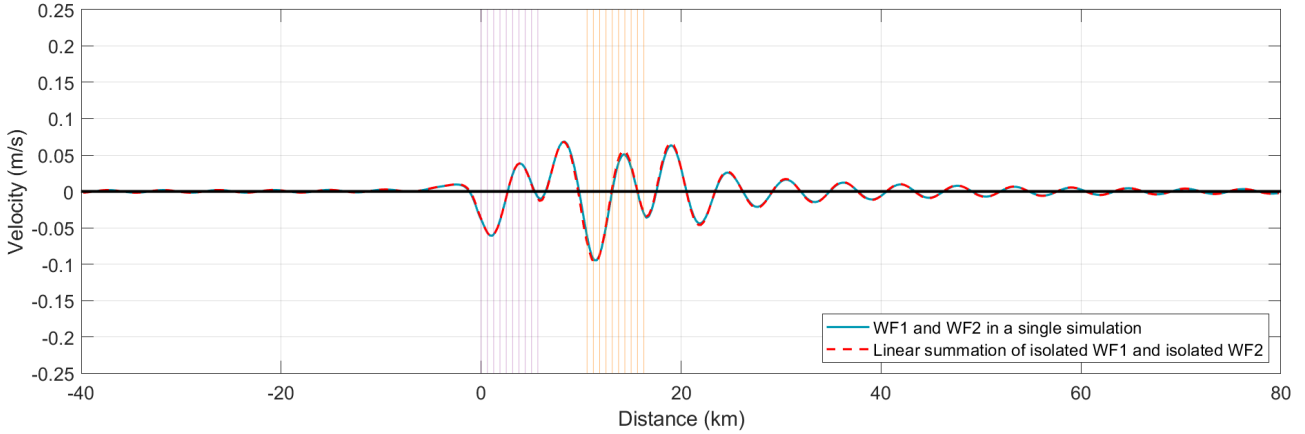


Figure 5.10: The Lee wave effect for the linear superposition of the single isolated wind farm simulation and the combined wind farm simulations, for a wind farm distance of 39.1D. The wind farm rows are visible as vertical lines.

The Lee wave effect of WF1 damps out quickly downstream of WF1. Consequently, there is little interaction between WF1 and WF2. Furthermore, the Lee wave effect downstream of WF2 is also small, which makes the overall behaviour look more linear. To see whether this linear relation holds for smaller wind farm distancing, 9.7D is plotted in Figure 5.11.

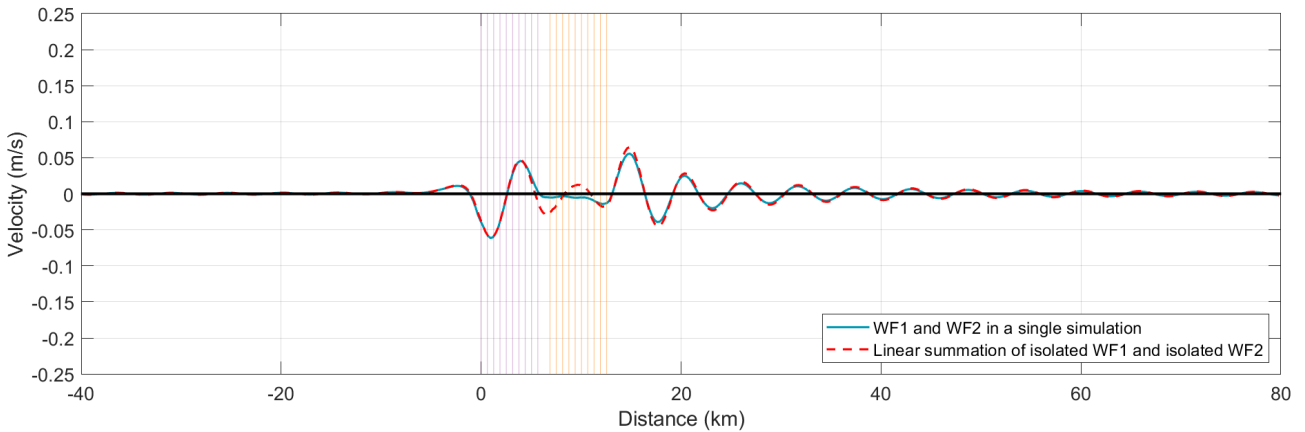


Figure 5.11: The Lee wave effect for the linear superposition of the single isolated wind farm simulation and the combined wind farm simulations, for a wind farm distance of 9.7D. The wind farm rows are visible as vertical lines.

As shown, this linear relation no longer holds. While a detailed analysis of the Lee wave effect fitting was considered, the combination of its harmonic behaviour, limited interaction distances, and relatively small magnitude made it hard to find a similar relation as for the dominant inversion layer displacement effect.

5.4 Power production

This subsection presents the analysis of the power output of the wind farms. The power output for each turbine is calculated using Equation (10), where the wind speed is the individual turbine velocity at hub height for both the TNBL and CNBL simulations separately.

$$P = \frac{1}{2} \rho A v^3 C_P \quad (10)$$

where:

P : Power output (W)

ρ : Air density (kg/m^3)

A : Rotor swept area (m^2)

v : Wind speed (m/s)

C_P : Power coefficient (-)

Note that C_P is iteratively changed as explained in Section 3.2. With this formula, the power output can be calculated, which has been done in Figure 5.12 for both the TNBL and CNBL simulation. In Figure 5.12a, one can see the row averaged velocity, and in Figure 5.12b, the row averaged wind turbine power output.

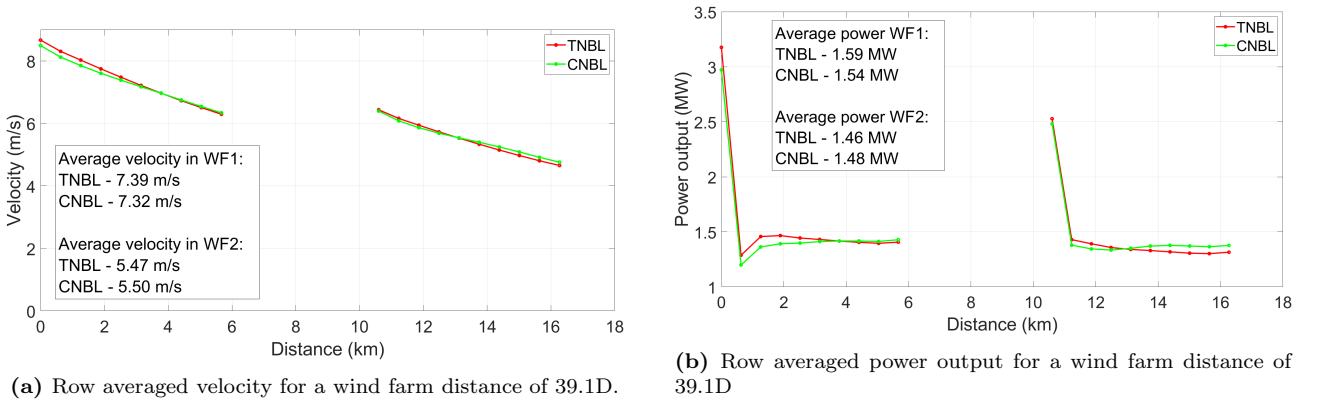


Figure 5.12: Row averaged velocity and power output for a wind farm distance of 39.1D

In Figure 5.12a, one can again see the CNBL effects when comparing the TNBL and CNBL velocity profiles. There is global blockage near the start of the wind farm and a speed up near the end. Furthermore, the average velocity over the whole wind farm is calculated and shown in the figure. In general, one expects that the CNBL effects have a negative effect on an isolated wind farm. Thus, a lower wind velocity is expected. For WF1, the average velocity for the TNBL simulation is indeed larger compared to the CNBL simulation. Still, for WF2, one can see that the average velocity for the TNBL simulation is smaller than the CNBL simulation. The reason for this is that WF2 benefits from the speed-up effect of WF1, which extends beyond its boundaries.

The same behaviour is shown in Figure 5.12a for the power output. It is important to note that the power output trend of WF2 is unexpected as the power output of the TNBL simulation does not recover after the first wind turbine as visible in WF1. This unexpected pattern occurs for wind farm distances below 81.2D (not shown in this report). Even though other studies have shown similar power output trends within wind farms (Nygaard, 2014; Nygaard & Hansen, 2016), most parameter spaces show a trend similar to WF1 (Lanzilao & Meyers, 2023).

To investigate how WF1 affects the power output of WF2 only regarding the CNBL effects and the other way around, the power output of WF1, WF2, and WF1 + WF2 for multiple distances are analysed for the TNBL simulation and CNBL simulation. The result is shown in Figure 5.13.

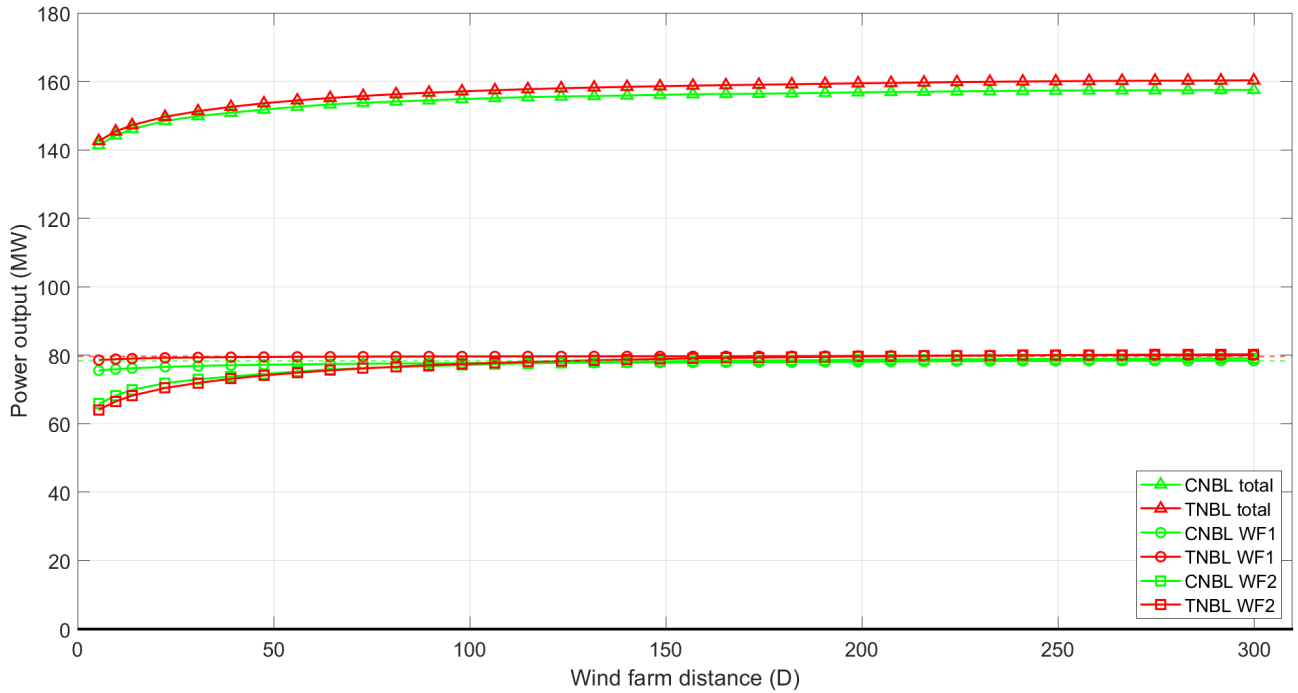


Figure 5.13: Power output per wind farm and combined for TNBL and CNBL as a function of wind farm distancing. The thin dashed line indicates the power output of a single isolated wind farm for TNBL and CNBL.

Analysing the TNBL simulations, one can see that the combined power production of WF1 and WF2 decreases as the wind farm distance decreases due to the wake effects. By analysing the individual TNBL power production for WF1 and WF2, one can see that the decrease in total power output is only due to WF2. It is interesting to see that the power output of WF1 also decreases slightly, which could be explained by the local blockage effect of WF2 that interacts with WF1. As shown in Figure 5.1, the local blockage effect starts approximately at 5 km or 40D upstream of WF1. This is approximately where the TNBL power output of WF1 in Figure 5.13 starts to decrease slightly.

Looking at how the CNBL total power output differs from the TNBL total power output for largely distanced wind farms, one can see that the CNBL effects reduce power production. Both WF1 and WF2 have a similar decrease in power output compared to a TNBL, due to stronger global blockage effects at the start of each wind farm despite a small speed-up towards the end of the farm. For smaller wind farm distancing, the total power output still experiences a decrease in power output, but less than for large wind farm distancing. Looking at the individual power output of WF1 and WF2, one can see an interesting relation. The CNBL power output of WF2, for wind farm distancing of $\pm 72D$, is larger than the TNBL power output. The reason for this is that it benefits from the speed-up effect of WF1. For WF1, the gap between CNBL and TNBL power output increases for smaller wind farm distancing, but this rate of change is lower than the rate at which the CNBL power output of WF2 surpasses the TNBL output for small wind farm distancing. This results in converging the total power output curves for CNBL and TNBL simulations for smaller wind farm distancing.

Another way to quantify the CNBL effects better, is to set the TNBL power output for WF1, WF2, and WF1+WF2 as a reference level at 100%, and compare it to the CNBL output. This has been done in Figure 5.14.

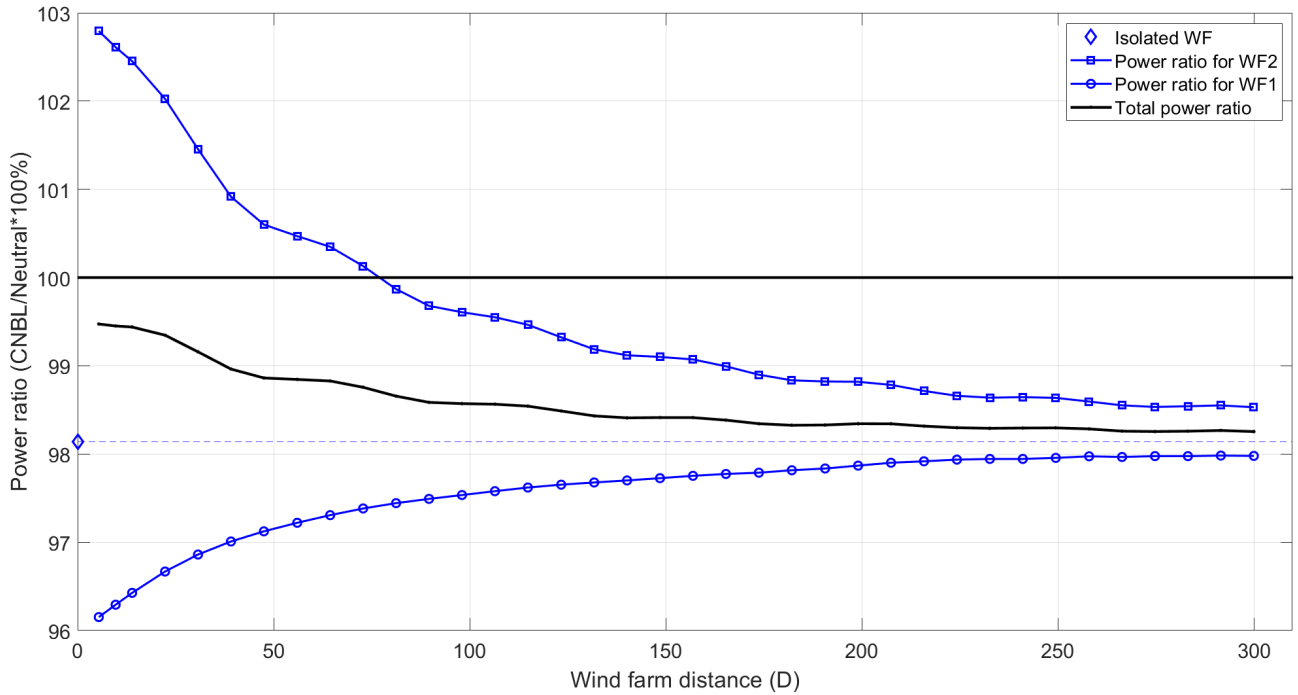


Figure 5.14: A comparison between the power output of a TNBL and CNBL simulation for WF1, WF2 and the total, as a function of wind farm distancing, with TNBL as a reference at 100%. The diamond marker with horizontal dashed line indicates the decrease in power output for a single isolated wind farm, in a CNBL compared to a TNBL.

For infinitely distanced wind farms, the total power production for CNBL is lower than the TNBL power production as mentioned before. Figure 5.14 shows that for an isolated wind farm, the CNBL power output is 98.1% of the TNBL output. As expected, the power ratios for WF1, WF2, and total power converge to this value at large wind farm distancing. The total power ratio remains below 100%, indicating that for all wind farm distancing, the CNBL effects reduce the overall power production compared to TNBL conditions. However, this negative impact decreases as wind farm distancing decreases. This relation can be explained by analysing the power ratios of the individual wind farms. WF2 experiences an increasingly strong speed-up effect from WF1, causing the power output to exceed the TNBL power output at wind farm distances below $\pm 75D$. In contrast, WF1 experiences an increasingly stronger blockage effect from WF2 at smaller wind farm distances, further reducing its power output compared to the TNBL power output.

It is important to note that this does not mean that the wind farms should be positioned as close together as possible because the wake effect of WF1 on WF2 decreases power output much more than the benefits from the CNBL effects as shown in Figure 5.13. The wake effects result in a decrease in TNBL power output of WF1, of around 20% for small wind farm distances compared to infinitely distanced wind farms, while the "positive" CNBL effects for small wind farm distances do not reach 3% for WF2 for the smallest wind farm distances. This is also visible in Figure 5.13, where you see the power output decrease in both TNBL and CNBL simulations. In contrast to suggestions minimal distance between wind farms, these results show that the wake effects in this parameter space are less severe than predicted by TNBL simulations alone. Lastly, it is visible that WF2 has more harmonic fluctuations due to the Lee wave effect because the Lee wave effect of WF1 also acts inside WF2, creating constructive or destructive interference. Its effect only cause small fluctuations in power output, but this could change for other parameter spaces where the wavelength of the Lee wave effect is different than the length of the wind farm.

6 Conclusion

This study investigates the aerodynamic interaction between two neighbouring offshore wind farms operating in a CNBL where the ABL is neutrally stable, capped by a stable inversion layer, and a less stable free atmosphere above. We compare the performance of the two wind farms in a CNBL to that in a TNBL with neutral conditions throughout the ABL and above for a set parameter space. $Fr_i = 1$ as this enhances the CNBL effects.

RQ1: The CNBL develops when steady winds move over a surface of constant temperature, for example, the sea. Then, the combined induction effects of the wind turbines cause an increased pressure, which deflects the wind flow vertically and laterally around the wind farm. The vertical component interacts with the inversion layer, a thin atmospheric layer characterized by an abrupt temperature increase to maintain equilibrium with the free atmosphere, and deforms the inversion layer. This results in three-dimensional internal AGWs in the free atmosphere and two-dimensional interfacial AGWs within the inversion layer. The initial dominant displacement of the inversion layer is called the dominant inversion layer displacement effect. At the end of the wind farm, the descending wind flow pulls the inversion layer down towards the wake region with low pressure. The vertical displacement of the inversion layer upstream and downstream of the wind farm creates an extra high and low-pressure zone, which reduces the wind speed at the start of the wind farm and accelerates it towards the end. Due to the displacement of the inversion layer, an oscillating wave forms in the inversion layer referred to as the Lee wave effect in this study.

RQ2: Both CNBL effects, the dominant inversion layer displacement effect and the Lee wave effect, create a larger response downstream than upstream, meaning that the speed-up works further downstream than the global blockage upstream. This asymmetric behaviour is small for the dominant inversion layer displacement effect and large for the Lee wave effect.

A key finding is that the global blockage and speed-up interaction between two wind farms cannot be predicted through linear superposition of individual wind farm CNBL effects. The dominant inversion layer displacement effect of WF2 is small upstream of WF1, and the dominant inversion layer displacement effect of WF1 is mild downstream of WF2. This means that most interaction takes place between the start of WF1 and the end of WF2. Furthermore, the Lee wave effects show complex harmonic wave interactions. This, in combination with the fact that the upstream and downstream effects damp out fast, makes it hard to analyse this. It is observed that the interaction of internal AGWs creates constructive and destructive interference that further complicates the Lee wave effects. In addition, the wavelength of the Lee wave effect in this parameter space (i.e., $Fr = 0.10$, $Fr_i = 1.0$, $\tilde{H}_i = 500m$, and $L_f = 5.67km$) is approximately the same as the length of the wind farm, which causes small effects on the power output.

RQ3: Multiple conclusions can be made when comparing a reference TNBL power output (set at 100%), for WF1, WF2, and total power output of both wind farms, to a CNBL power output for different wind farm distances. It has been found that for infinitely distanced wind farms in this parameter space, the CNBL effects are negative due to stronger global blockage effects at the start of the wind farm despite a small speed-up towards the end of the farm. The CNBL simulation power output is therefore 98.1% of the TNBL simulation. However, for smaller wind farm spacings, the downstream effects dominate upstream effects in between the wind farms. This means that the speed-up effect induced by WF1 proves to be stronger than the global blockage effect of WF2, leading to benefits for WF2. For wind farm distances below $\pm 72D$, the power output of WF2 in a CNBL is larger than the power output of WF2 in a TNBL. In contrast, WF1 experiences a negative effect of WF2, which results in an even lower power output than 98.1%. For a wind farm distance of 25D, WF1 has a CNBL power output of 96.7% of the TNBL power output, while WF2 has a CNBL power output of 101.8%. Even the total power output of both wind farms in CNBL reaches a value higher than 98.1% compared to the TNBL power output, with a value of 99.3% for a wind farm distance of 25D.

RQ4: As explained, this means that a TNBL simulation generally overestimates the power output of an isolated wind farm in a CNBL, but this does not always apply to clustered wind farms. Lastly, it is not a good idea to position the wind farms as close together. While it has been found that WF1 results in an increase of the power output regarding only the CNBL effects, the benefits created should be weighed against the still dominant wake effects. Putting the wind farms very close together results in wake effects of around 20% in a TNBL simulation for WF2. While the CNBL effects do decrease this percentage slightly by $\pm 3\%$, it will not be beneficial to place them close together.

The findings have direct effects on offshore planning. As offshore wind development continues to expand with large-scale wind farms being planned in a small area, this research provides important insights into how the power output could be under or over-predicted depending on the wind farm distancing and atmospheric conditions.

7 Discussion and recommendation

This study shows important findings for the development of offshore wind farms. It has been shown by other studies that the CNBL effects generally have negative effects on the power production. This study shows that the downstream wind farm could profit from the speed up of the upstream wind farm, more than its own negative effects. Wind farm operators can by reading this study get a first estimate in what the CNBL effects would be for the power production of their wind farm, dependent on whether the wind farm is downstream or upstream. In this section, a few discussion points about the method, assumptions and model will be mentioned.

Method: MSC was used to perform this study due to its relatively short simulation time and to capture both meso and micro-scale effects. This was key to investigate many wind farm distances. Even though this approach proved to be very accurate, the results could still be slightly off. In Stipa, Ajay, et al. (2024), it was shown that MSC underestimated wind farm power by about only 2% compared with the LES results.

In this paper it was chosen to quantify the CNBL effects by subtracting the velocity profile of the TNBL from the CNBL simulation. Another approach would be to regard the background velocity, which also shows the CNBL effects. The velocity profiles from both methods show similar overall relationships, with only small differences between them. In general, the background velocity method appears to have a slightly larger blockage effect, which means it would be interesting to see how the velocity analysis in this paper will differ with this method in future research. This will not affect the power output.

Additionally, settings are chosen in MSC which have a fast simulation time, while keeping its accuracy as good as possible. There are settings that better simulate the far wake effects, but its effects are small while increasing the computation time significantly. Lastly, the Nieuwstadt model could cause small deviations from the initially specified Froude numbers.

Assumptions: There are multiple assumptions made by choosing MSC as explained in Section 3.2, like scale separation, periodic boundary layers, height averaged per layer, incompressible flow. Next to the model assumptions, it is also assumed that the parameters like inversion layer height, lapse rate, wind velocity and wind direction are constant. Realistically, these vary in time which could impose other challenges such as the interaction of the turbine blades with the inversion layer. Furthermore, no Coriolis force is assumed and a surface roughness of 0.1 mm which is common for a calm sea, while other studies recommend 0.2 mm or higher (Y. He et al., 2021). The surface roughness is an important parameter, as a higher surface roughness results in a smaller inversion layer displacement which could decrease the CNBL effects discussed in this study.

Future research: Future research should explore with LES simulations what the CNBL effects are when changing the Froude number. This could be interesting because previous research showed that this could result in an increase in power output due to the CNBL effects and this study showed that when wind farms are placed less than $72D$ apart, the downstream speed up effect dominates over the upstream global blockage effects. These results could differ because the high and low pressure areas could shift upstream/downstream for different Froude numbers, interfering with the downstream/upstream wind farm. The LES simulations will show more insights such as the transient phase and a vertical velocity profile and has a higher accuracy compared to MSC. Furthermore other turbine types and farm layouts should also be studied. Also validation against measurements in the field would be needed in the future. Lastly, it would be interesting to see what would happen when simulating a varying wind direction and velocity, which would result in a more realistic power output.

Limitations: The wavelength of Lee wave matching the wind farm length in this parameter space may have reduced Lee wave effect visible in the power output. Different parameter spaces could show larger effects, because the wavelength of the Lee wave would then differ from the length of the wind farm. Another limitation by the choice of MSC is that one could not give the reason behind the Lee wave effect because no vertical velocity profile is resolved, as the model uses depth-averaged quantities in each layer. Lastly, the power output of the second wind farm in Figure 5.12a has an unexpected shape for small wind farm distances. Due to the limited MSC studies done on two wind farms, it should be verified with LES simulations.

References

- Abkar, M., & Porté-Agel, F. (2013, 4). The Effect of Free-Atmosphere Stratification on Boundary-Layer Flow and Power Output from Very Large Wind Farms. *Energies 2013, Vol. 6, Pages 2338-2361*, 6(5), 2338–2361. Retrieved from <https://www.mdpi.com/1996-1073/6/5/2338/htm><https://www.mdpi.com/1996-1073/6/5/2338> doi: 10.3390/EN6052338
- Abkar, M., & Porté-Agel, F. (2014). The effect of atmospheric stability on wind-turbine wakes: A large-eddy simulation study. *Journal of Physics: Conference Series*, 524(1). doi: 10.1088/1742-6596/524/1/012138
- Abkar, M., & Porté-Agel, F. (2015, 3). Influence of atmospheric stability on wind-turbine wakes: A large-eddy simulation study. *Physics of Fluids*, 27(3). doi: 10.1063/1.4913695
- Allaerts, D. (2016, 11). *Large-eddy Simulation of Wind Farms in Conventionally Neutral and Stable Atmospheric Boundary Layers*. Retrieved from https://www.researchgate.net/publication/321171743_Large-eddy_Simulation_of_Wind_Farms_in_Conventionally_Neutral_and_Stable_Atmospheric_Boundary_Layers
- Allaerts, D., Broucke, S. V., Van Lipzig, N., & Meyers, J. (2018, 6). Annual impact of wind-farm gravity waves on the Belgian-Dutch offshore wind-farm cluster. *Journal of Physics: Conference Series*, 1037(7). Retrieved from https://www.researchgate.net/publication/325831861_Annual_impact_of_wind-farm_gravity_waves_on_the_Belgian-Dutch_offshore_wind-farm_cluster doi: 10.1088/1742-6596/1037/7/072006
- Allaerts, D., & Meyers, J. (2015, 6). Large eddy simulation of a large wind-turbine array in a conventionally neutral atmospheric boundary layer. *Physics of Fluids*, 27(6). Retrieved from https://www.researchgate.net/publication/279740428_Large_eddy_simulation_of_a_large_wind-turbine_array_in_a_conventionally_neutral_atmospheric_boundary_layer doi: 10.1063/1.4922339
- Allaerts, D., & Meyers, J. (2017, 3). Boundary-layer development and gravity waves in conventionally neutral wind farms. *Journal of Fluid Mechanics*, 814, 95–130. Retrieved from https://www.researchgate.net/publication/313414818_Boundary-layer_development_and_gravity_waves_in_conventionally_neutral_wind_farms doi: 10.1017/JFM.2017.11
- Allaerts, D., & Meyers, J. (2019, 3). Sensitivity and feedback of wind-farm induced gravity waves. *Journal of fluid mechanics*, 862, 990. Retrieved from [/pmc/articles/PMC6436732//pmc/articles/PMC6436732/?report=abstract](https://www.ncbi.nlm.nih.gov/pmc/articles/PMC6436732/)<https://www.ncbi.nlm.nih.gov/pmc/articles/PMC6436732/> doi: 10.1017/JFM.2018.969
- Baas, P., Verzijlbergh, R., Van Dorp, P., & Jonker, H. (2023, 5). Investigating energy production and wake losses of multi-gigawatt offshore wind farms with atmospheric large-eddy simulation. *Wind Energy Science*, 8(5), 787–805. doi: 10.5194/WES-8-787-2023
- Brost, R. A., Lenschow, D. H., & Wyngaard J. C. (1982, 4). *Marine Stratocumulus Layers. Part 1: Mean Conditions in: Journal of the Atmospheric Sciences Volume 39 Issue 4*. Retrieved from https://journals.ametsoc.org/view/journals/atsc/39/4/1520-0469_1982_039_0800_ms1pmc_2_0_co_2.xml
- Cañadillas, B., Foreman, R., Barth, V., Siedersleben, S., Lampert, A., Platis, A., ... Neumann, T. (2020, 5). Offshore wind farm wake recovery: Airborne measurements and its representation in engineering models. *Wind Energy*, 23(5), 1249–1265. doi: 10.1002/WE.2484
- Cao, J., Qin, Z., Gao, X., Pu, T., Zhu, W., Ke, S., & Shen, X. (2023, 7). Study of aerodynamic performance and wake effects for offshore wind farm cluster. *Ocean Engineering*, 280, 114639. Retrieved from <https://www.sciencedirect.com/science/article/pii/S0029801823010235> doi: 10.1016/J.OCEANENG.2023.114639
- Draxl, C., Worsnop, R. P., Xia, G., Pichugina, Y., Chand, D., Lundquist, J. K., ... Berg, L. K. (2020). Mountain waves can impact wind power generation. *Wind Energ. Sci*, 6, 2021. Retrieved from <https://doi.org/10.5194/wes-6-45-2021> doi: 10.5194/wes-6-45-2021
- Durrán, D. R. (1990). Mountain Waves and Downslope Winds. *Atmospheric Processes over Complex Terrain*. Retrieved from https://link.springer.com/chapter/10.1007/978-1-935704-25-6_4 doi: 10.1007/978-1-935704-25-6{-}4
- Durrán, D. R., & Klemp, J. B. (1987, 11). *Another Look at Downslope Winds. Part II: Nonlinear Amplification beneath Wave-Overtaking Layers in: Journal of the Atmospheric Sciences Volume 44 Issue 22 (1987)*. Retrieved from https://journals.ametsoc.org/view/journals/atsc/44/22/1520-0469_1987_044_3402_aladwp_2_0_co_2.xml
- Dutra, E., Muñoz-Sabater, J., Boussetta, S., Komori, T., Hirahara, S., & Balsamo, G. (2020, 5). Environmental Lapse Rate for High-Resolution Land Surface Downscaling: An Application to ERA5. *Earth and Space Science*, 7(5), e2019EA000984. Retrieved from <https://onlinelibrary.wiley.com/doi/full/10.1029/2019EA000984>

- 2019EA000984<https://onlinelibrary.wiley.com/doi/abs/10.1029/2019EA000984><https://agupubs.onlinelibrary.wiley.com/doi/10.1029/2019EA000984> doi: 10.1029/2019EA000984
- Energy Watch. (2022). *Danish offshore wind to quintuple by 2030*. Retrieved from <https://energywatch.com/EnergyNews/Policy---Trading/article14139797.ece>
- Feliciano, J., Cortina, G., Spear, A., & Calaf, M. (2018, 5). Generalized analytical displacement model for wind turbine towers under aerodynamic loading. *Journal of Wind Engineering and Industrial Aerodynamics*, 176, 120–130. doi: 10.1016/J.JWEIA.2018.03.018
- Gill, A. (1982, 11). *Atmosphere-Ocean Dynamics, Volume 30 - 1st Edition*. Retrieved from <https://shop.elsevier.com/books/atmosphere-ocean-dynamics/gill/978-0-12-283522-3>
- Grant, A. L. (1986, 7). Observations of boundary layer structure made during the 1981 KONTUR experiment. *Quarterly Journal of the Royal Meteorological Society*, 112(473), 825–841. Retrieved from <https://onlinelibrary.wiley.com/doi/full/10.1002/qj.49711247314><https://onlinelibrary.wiley.com/doi/abs/10.1002/qj.49711247314><https://rmets.onlinelibrary.wiley.com/doi/10.1002/qj.49711247314> doi: 10.1002/QJ.49711247314
- Gupta, N. (2016, 6). A review on the inclusion of wind generation in power system studies. *Renewable and Sustainable Energy Reviews*, 59, 530–543. Retrieved from https://www.researchgate.net/publication/291348908_A_review_on_the_inclusion_of_wind_generation_in_power_system_studies_Elsevier-Impact_Factor-.10556 doi: 10.1016/J.RSER.2016.01.009
- Hansen, K. S., Réthoré, P. E., Palma, J., Hevia, B. G., Prospathopoulos, J., Peña, A., ... Volker, P. (2015, 6). Simulation of wake effects between two wind farms. *Journal of Physics: Conference Series*, 625(1). Retrieved from https://www.researchgate.net/publication/279071052_Simulation_of_wake_effects_between_two_wind_farms doi: 10.1088/1742-6596/625/1/012008
- Hasager, C. B., Vincent, P., Badger, J., Badger, M., Di Bella, A., Peña, A., ... Volker, P. J. (2015, 6). Using Satellite SAR to Characterize the Wind Flow around Offshore Wind Farms. *Energies* 2015, Vol. 8, Pages 5413-5439, 8(6), 5413–5439. Retrieved from <https://www.mdpi.com/1996-1073/8/6/5413/htm><https://www.mdpi.com/1996-1073/8/6/5413> doi: 10.3390/EN8065413
- He, F., Wagner, M., Zhang, L., Shao, C., Xu, W., Chen, W., ... Li, Y. (2022, 12). A novel integrated approach for offshore wind power optimization. *Ocean Engineering*, 266, 112827. doi: 10.1016/J.OCEANENG.2022.112827
- He, Y., Fu, J., Chan, P. W., Li, Q., Shu, Z., & Zhou, K. (2021, 7). Reduced Sea-Surface Roughness Length at a Coastal Site. *Atmosphere* 2021, Vol. 12, Page 991, 12(8), 991. Retrieved from <https://www.mdpi.com/2073-4433/12/8/991/htm><https://www.mdpi.com/2073-4433/12/8/991> doi: 10.3390/ATMOS12080991
- Inoue, M., Matheou, G., & Teixeira, J. (2014, 9). LES of a Spatially Developing Atmospheric Boundary Layer: Application of a Fringe Method for the Stratocumulus to Shallow Cumulus Cloud Transition. *Monthly Weather Review*, 142(9), 3418–3424. Retrieved from <https://journals.ametsoc.org/view/journals/mwre/142/9/mwr-d-13-00400.1.xml> doi: 10.1175/MWR-D-13-00400.1
- Jonkman, J., Butterfield, S., Musial, W., & Scott, G. (2009, 2). *Definition of a 5-MW Reference Wind Turbine for Offshore System Development* (Tech. Rep.). Retrieved from <http://www.osti.gov/bridge>
- Kollwitz, J., Liléo, S., & Ivanell, S. (2016, 10). *Defining the wake decay constant as a function of turbulence intensity to model wake losses in onshore wind farms*. Retrieved from https://windeurope.org/summit2016/conference/allfiles2/358_WindEurope2016presentation.pdf
- Lanzilao, L., & Meyers, J. (2022, 6). Effects of self-induced gravity waves on finite wind-farm operations using a large-eddy simulation framework. *Journal of Physics: Conference Series*, 2265(2). Retrieved from https://www.researchgate.net/publication/361038442_Effects_of_self-induced_gravity_waves_on_finite_wind-farm_operations_using_a_large-eddy_simulation_framework doi: 10.1088/1742-6596/2265/2/022043
- Lanzilao, L., & Meyers, J. (2023, 6). A parametric large-eddy simulation study of wind-farm blockage and gravity waves in conventionally neutral boundary layers. *Journal of Fluid Mechanics*, 979, A54. Retrieved from https://www.researchgate.net/publication/371605520_A_parametric_large-eddy_simulation_study_of_wind-farm_blockage_and_gravity_waves_in_conventionally_neutral_boundary_layers doi: 10.1017/JFM.2023.1088
- Long, R. R. (1953, 2). Some Aspects of the Flow of Stratified Fluids: I. A Theoretical Investigation. *Tellus*, 5(1), 42–58. Retrieved from <https://onlinelibrary.wiley.com/doi/full/10.1111/j.2153-3490.1953.tb01035.x><https://onlinelibrary.wiley.com/doi/abs/10.1111/j.2153-3490.1953.tb01035.x><https://onlinelibrary.wiley.com/doi/10.1111/j.2153-3490.1953.tb01035.x> doi: 10.1111/J.2153-3490.1953.TB01035.X
- Lott, F. (1998). Linear mountain drag and averaged pseudo-momentum flux profiles in the presence of trapped

- lee waves. *Tellus A: Dynamic Meteorology and Oceanography*, 50(1), 12–25. Retrieved from <https://www.tandfonline.com/doi/abs/10.3402/tellusa.v50i1.14509> doi: 10.3402/TELLUSA.V50I1.14509
- Maas, O. (2023, 4). From gigawatt to multi-gigawatt wind farms: wake effects, energy budgets and inertial gravity waves investigated by large-eddy simulations. *Wind Energy Science*, 8(4), 535–556. doi: 10.5194/WES-8-535-2023
- Maas, O., & Raasch, S. (2022, 3). Wake properties and power output of very large wind farms for different meteorological conditions and turbine spacings: A large-eddy simulation case study for the German Bight. *Wind Energy Science*, 7(2), 715–739. Retrieved from https://www.researchgate.net/publication/354098470.Wake_properties_and_power_output_of_very_large_wind_farms_for_different_meteorological_conditions_and_turbine_spacings_A_large-eddy_simulation_case_study_for_the_German_Bight doi: 10.5194/WES-7-715-2022
- Nappo, C. J. (2012). The Hydrostatic Atmosphere. *International Geophysics*, 102, 309–321. doi: 10.1016/B978-0-12-385223-6.00011-2
- Nastrom, G. D., & Fritts, D. C. (1992, 1). *Sources of Mesoscale Variability of Gravity Waves. Part I: Topographic Excitation in: Journal of the Atmospheric Sciences Volume 49 Issue 2*. Retrieved from https://journals.ametsoc.org/view/journals/atsc/49/2/1520-0469_1992_049_0101_somvog_2_0_co_2.xml
- Nygaard, N. G. (2014). Wakes in very large wind farms and the effect of neighbouring wind farms. *Journal of Physics: Conference Series*, 524(1). doi: 10.1088/1742-6596/524/1/012162
- Nygaard, N. G., & Hansen, S. D. (2016, 9). Wake effects between two neighbouring wind farms. *Journal of Physics: Conference Series*, 753(3), 032020. Retrieved from <https://iopscience.iop.org/article/10.1088/1742-6596/753/3/032020> doi: 10.1088/1742-6596/753/3/032020
- Office of energy efficiency & renewable energy. (2024, 4). *From 1970s Pioneers to Today's Wind Industry, Aerospace Researchers Championed Wind Energy — Department of Energy*. Retrieved from <https://www.energy.gov/eere/wind/articles/1970s-pioneers-todays-wind-industry-aerospace-researchers-championed-wind-energy>
- Ollier, S. J., Watson, S. J., & Montavon, C. (2018, 6). Atmospheric gravity wave impacts on an offshore wind farm. *Journal of Physics: Conference Series*, 1037(7). Retrieved from https://www.researchgate.net/publication/325835737_Atmospheric_gravity_wave_impacts_on_an_offshore_wind_farm doi: 10.1088/1742-6596/1037/7/072050
- Paul Van Der Laan, M., & Nørmark Sørensen, N. (2017). Why the Coriolis force turns a wind farm wake clockwise in the Northern Hemisphere. *Wind Energy Science*, 2(1), 285–294. doi: 10.5194/WES-2-285-2017
- Platis, A., Siedersleben, S. K., Bange, J., Lampert, A., Bärfuss, K., Hankers, R., ... Emeis, S. (2018, 2). First in situ evidence of wakes in the far field behind offshore wind farms. *Scientific Reports 2018 8:1*, 8(1), 1–10. Retrieved from <https://www.nature.com/articles/s41598-018-20389-y> doi: 10.1038/s41598-018-20389-y
- Queney, P. (1948, 1). The Problem of Air Flow Over Mountains: A Summary of Theoretical Studies. *Bulletin of the American Meteorological Society*, 29(1), 16–26. Retrieved from https://journals.ametsoc.org/view/journals/bams/29/1/1520-0477-29_1_16.xml doi: 10.1175/1520-0477-29.1.16
- Rijksoverheid. (2021). *Windenergiegebied Borsssele - Noordzeeloket*. Retrieved from <https://www.noordzeeloket.nl/functies-gebruik/windenergie/doorvaart-medegebruik/borsssele/>
- Schneemann, J., Rott, A., Dörenkämper, M., Steinfeld, G., & Kühn, M. (2020, 1). Cluster wakes impact on a far-distant offshore wind farm's power. *Wind Energy Science*, 5(1), 29–49. doi: 10.5194/WES-5-29-2020
- Scorer, R. S. (1949, 1). Theory of waves in the lee of mountains. *Quarterly Journal of the Royal Meteorological Society*, 75(323), 41–56. Retrieved from <https://onlinelibrary.wiley.com/doi/full/10.1002/qj.49707532308><https://onlinelibrary.wiley.com/doi/abs/10.1002/qj.49707532308><https://rmets.onlinelibrary.wiley.com/doi/10.1002/qj.49707532308> doi: 10.1002/QJ.49707532308
- Smith, R. B. (1980, 8). Linear theory of stratified hydrostatic flow past an isolated mountain. *Tellus*, 32(4), 348–364. Retrieved from <https://onlinelibrary.wiley.com/doi/full/10.1111/j.2153-3490.1980.tb00962.x><https://onlinelibrary.wiley.com/doi/abs/10.1111/j.2153-3490.1980.tb00962.x><https://onlinelibrary.wiley.com/doi/10.1111/j.2153-3490.1980.tb00962.x> doi: 10.1111/J.2153-3490.1980.TB00962.X
- Smith, R. B. (2010). Gravity wave effects on wind farm efficiency. *Wind Energy*, 13(5), 449–458. doi: 10.1002/WE.366
- Sorbjan, Z. (2003). *Air pollution meteorology*. Retrieved from https://www.researchgate.net/publication/228751584_Air_pollution_meteorology
- Stipa, S., Ajay, A., Allaerts, D., & Brinkerhoff, J. (2023, 5). *TOSCA - An Open-Source Finite-Volume LES Environment for Wind Farm Flows*. Retrieved from <https://www.researchgate.net/publication/>

370659234.TOSCA_-An_Open-Source_Finite-Volume_LES_Environment_for_Wind_Farm_Flows

- Stipa, S., Ajay, A., Allaerts, D., & Brinkerhoff, J. (2024, 5). The multi-scale coupled model: a new framework capturing wind farm-atmosphere interaction and global blockage effects. *Wind Energy Science*, 9(5), 1123–1152. doi: 10.5194/WES-9-1123-2024
- Stipa, S., Khan, M. A., Allaerts, D., & Brinkerhoff, J. (2024, 8). A large-eddy simulation (LES) model for wind-farm-induced atmospheric gravity wave effects inside conventionally neutral boundary layers. *Wind Energy Science*, 9(8), 1647–1668. Retrieved from https://www.researchgate.net/publication/361038442.Effects_of_self-induced_gravity_waves_on_finite_wind-farm_operations_using_a_large-eddy_simulation_framework doi: 10.5194/WES-9-1647-2024
- Talley, L. D., Pickard, G. L., Emery, W. J., & Swift, J. H. (2011). Physical Properties of Seawater. *Descriptive Physical Oceanography*, 29–65. doi: 10.1016/B978-0-7506-4552-2.10003-4
- Tjernstrom, M., & Smedman, A. S. (1993). The vertical turbulence structure of the coastal marine atmospheric boundary layer. *Journal of Geophysical Research*, 98(C3), 4809–4826. doi: 10.1029/92JC02610
- TNO. (2023). *Offshore wind energy deployment in the North Sea by 2030: long-term measurement campaign. EPL, 2016-2022*. Retrieved from <https://repository.tno.nl/SingleDoc?find=UID%207efd1ed6-65e5-43a7-895d-855663f6fc64>
- USGS. (2022, 2). *How many turbines are contained in the U.S. Wind Turbine Database? — U.S. Geological Survey*. Retrieved from <https://www.usgs.gov/faqs/how-many-turbines-are-contained-us-wind-turbine-database?>
- Van Der Laan, M. P., Hansen, K. S., Sørensen, N. N., & Réthoré, P. E. (2015, 6). Predicting wind farm wake interaction with RANS: An investigation of the Coriolis force. *Journal of Physics: Conference Series*, 625(1). Retrieved from https://www.researchgate.net/publication/279070973_Predicting_wind_farm_wake_interaction_with_RANS_an_investigation_of_the_Coriolis_force doi: 10.1088/1742-6596/625/1/012026
- Vattenfall. (2024). *Vattenfall sets circular economy target for permanent magnets - Vattenfall*. Retrieved from <https://group.vattenfall.com/press-and-media/newsroom/2024/vattenfall-sets-circular-economy-target-for-permanent-magnets>
- Veers, P., Dykes, K., Lantz, E., Barth, S., Bottasso, C. L., Carlson, O., ... Wisser, R. (2019, 10). Grand challenges in the science of wind energy. *Volume 366, Issue 6464, 366(6464)*. doi: 10.1126/science.aau2027
- Wind Europe. (2023). *Wind energy in Europe: 2023 Statistics and the outlook for 2024-2030 — WindEurope*. Retrieved from <https://windeurope.org/intelligence-platform/product/wind-energy-in-europe-2023-statistics-and-the-outlook-for-2024-2030/#overview>
- Wu, K. L., & Porté-Agel, F. (2017, 12). Flow Adjustment Inside and Around Large Finite-Size Wind Farms. *Energies 2017, Vol. 10, Page 2164, 10(12)*, 2164. Retrieved from <https://www.mdpi.com/1996-1073/10/12/2164/htmhttps://www.mdpi.com/1996-1073/10/12/2164> doi: 10.3390/EN10122164
- Wu, Y. T., & Porté-Agel, F. (2013, 2). Simulation of Turbulent Flow Inside and Above Wind Farms: Model Validation and Layout Effects. *Boundary-Layer Meteorology*, 146(2), 181–205. doi: 10.1007/S10546-012-9757-Y
- Yang, X., Howard, K. B., Guala, M., & Sotiropoulos, F. (2015, 2). Effects of a three-dimensional hill on the wake characteristics of a model wind turbine. *Physics of Fluids*, 27(2). doi: 10.1063/1.4907685
- Zilitinkevich, S., Esau, I., & Baklanov, A. (2007, 1). Further comments on the equilibrium height of neutral and stable planetary boundary layers. *Quarterly Journal of the Royal Meteorological Society*, 133(622), 265–271. Retrieved from <https://onlinelibrary.wiley.com/doi/full/10.1002/qj.27https://onlinelibrary.wiley.com/doi/abs/10.1002/qj.27https://rmets.onlinelibrary.wiley.com/doi/10.1002/qj.27> doi: 10.1002/QJ.27

Appendices

Appendix A MSC output figures

In Figure A.1 is the perturbation velocity shown, normalised with the average velocity in the wind farm layer in a CNBL for a wind farm distance of 39.1D. Looking at the upstream effects, the velocity perturbations shows a deceleration when approaching WF1. The region of deceleration in front and partially next to WF1 shows the global blockage effect, while at smaller scale the local blockage effects are visible. Furthermore, one can see a small thin deceleration around $y=0$. This is due to the fact that MSC recycles the wake profile at the end of the domain as explained in Section 3.2, but the perturbation is very small and assumed to be neglected. Inside WF1, a fast decrease of velocity can be seen due to the cumulative wakes of the wind turbines. After the significant decrease in velocity in WF1, a short wake recovery can be seen until WF2 where the same process as in WF1 is visible, except the large global blockage area which is significantly smaller. Furthermore, the wake effects behind WF2 are even larger than after WF1 due to the cumulative wake effect of two wind farms. It is also interesting to see that there is a small speed-up visible after WF2, outside of the wake region.

Looking at the pressure perturbation in Figure A.2, normalised by the dynamic pressure $\rho U b^2$ where ρ is the air density and $U b$ is the local background velocity in the wind farm and upper layer. Note that as the colorbar is ranging from -2% to 2.9%, the white colour is therefore around 0.3%. Upstream and partially adjacent to WF1 a large positive pressure perturbation is visible, indicating the global blockage effect. This global blockage effect extends relatively far into WF1 compared to WF2. In WF2, the global blockage effect is also smaller than in WF1. Downstream of WF1, a negative pressure perturbation is visible, while a much larger negative pressure perturbation can be seen within and downstream of WF2. The stronger perturbation behind WF2 is due to the cumulative effect of both wind farms. Lastly, the harmonic pattern behind WF2 shows clear signs of the Lee wave effect generated by the interaction between the wind farms and the stable atmosphere.

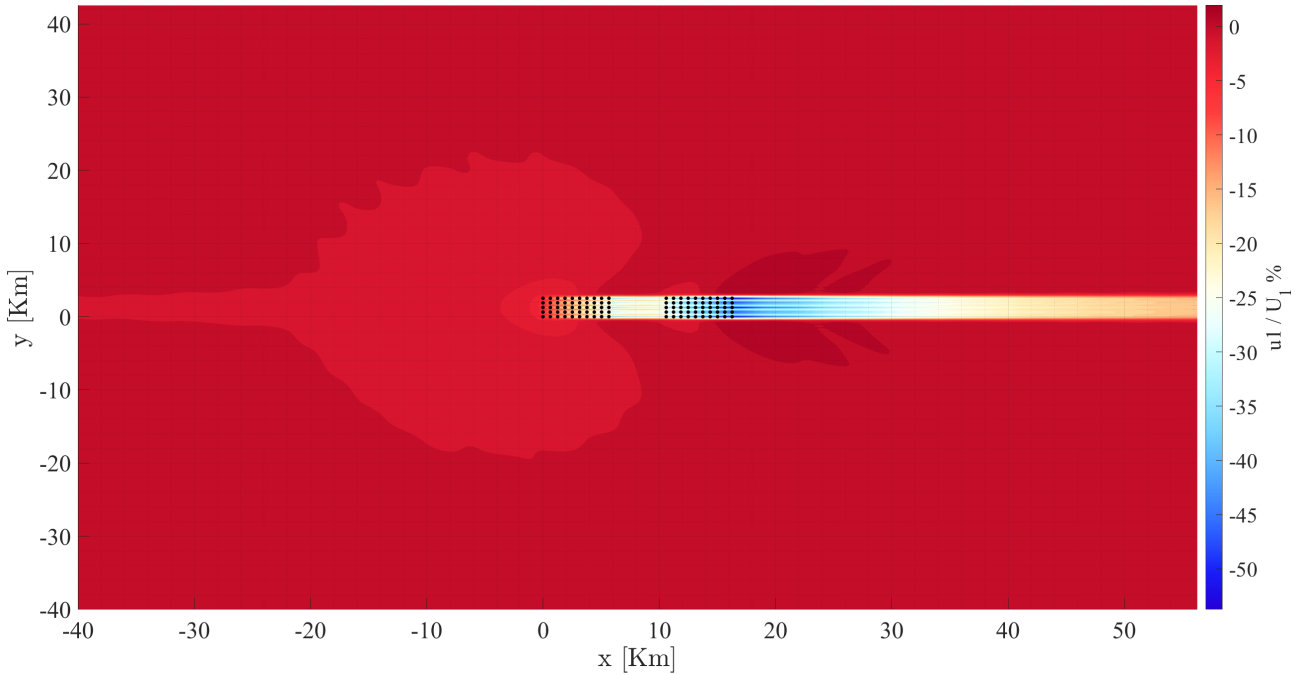


Figure A.1: Streamwise perturbation velocity u_1 at hub height, normalised with the average velocity in the wind farm layer, for two offshore wind farms separated by 39.1D in a CNBL

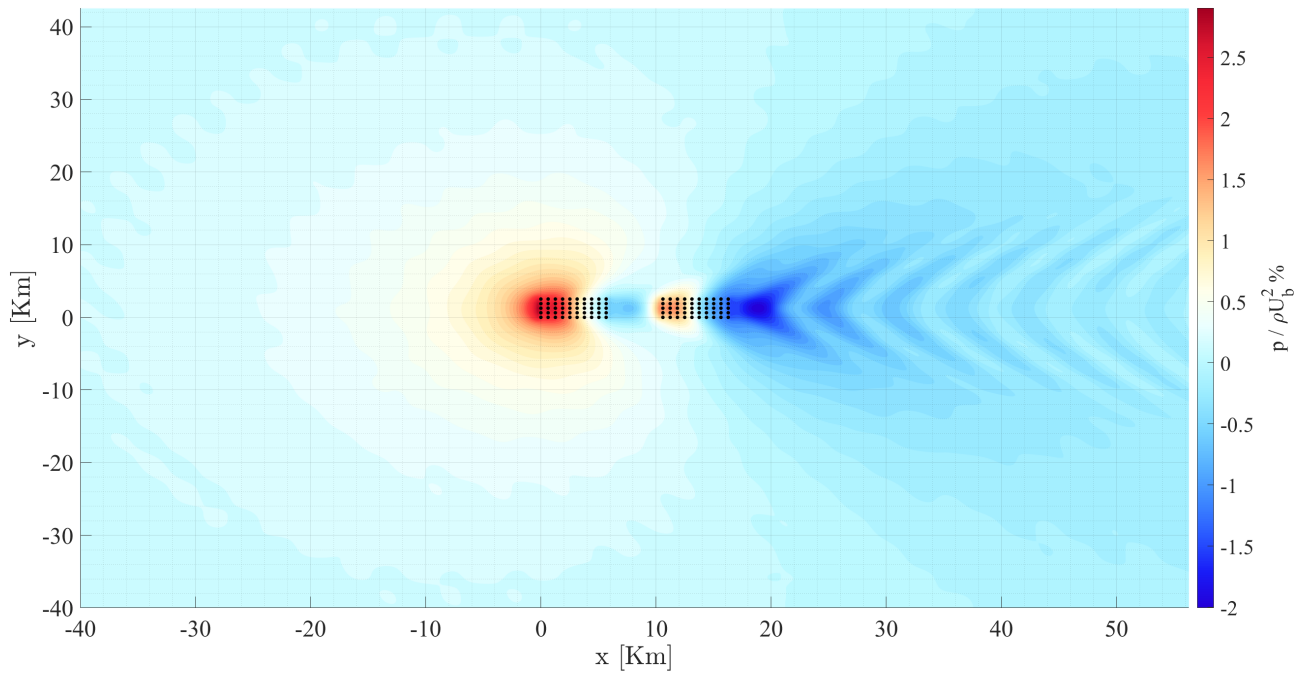


Figure A.2: Perturbation pressure p , normalised with the dynamic pressure, for two offshore wind farms separated by 39.1D in a CNBL

Appendix B The effect of the Deeparray parameter

When one subtracts the TNBL power output from the CNBL power output for WF1, WF2, and their total as shown in Figure 5.13, the absolute difference can be found. This has been done one time with the Deeparray parameter on and one time without. As visible, the differences between having the Deeparray parameter on or off are small.

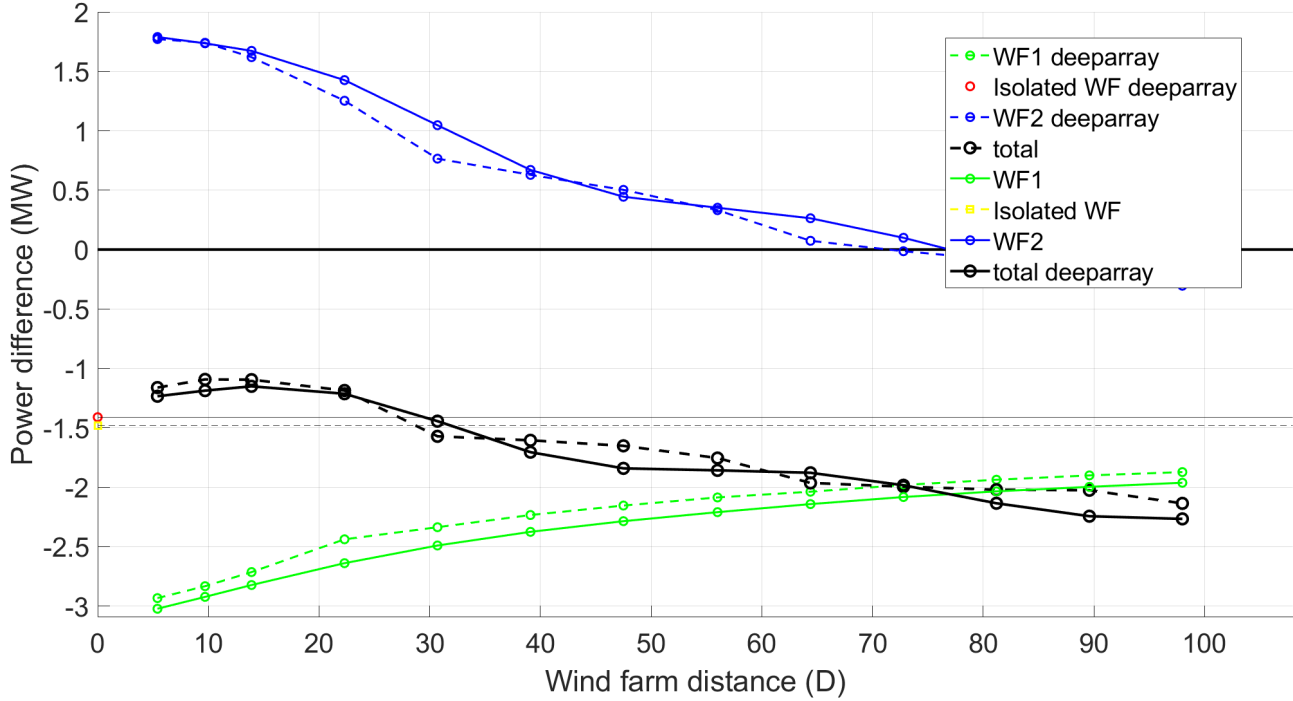


Figure B.1: The effect of the Deeparray parameter on the difference in power output between a TNBL and CNBL simulation, for WF1, WF2 and the total of both wind farms. Also the isolated single wind farm simulations are visible with dashed lines.

Appendix C MSC input

This is the MSC settings.msm input file and a overview of the content of the excel file N4.xlsm that is used in the MSC model.

Parameter	Value	Description
General Information		
File Type	settings.dw	
Reference Frame	Absolute	
Language	English	
Solution Controls		
iterations	3	Number of coupling iterations (min 1)
deepArray	0	Zero: none, Two: add deep array effects (only improves in random farm configurations + far wake)
localInduction	1	Add local turbine induction
readTurbineThrust	0	Thrust from LES (turbine thrust is fixed and uploaded from TOSCA turbine data)
readTurbineCtPrime	0	Disk-averaged thrust coefficient from LES (turbine CtPrime is fixed and uploaded from TOSCA turbine data)
periodicSpanwise	0	Periodize the wind turbine distribution in the spanwise direction (for laterally infinite wind farms)
ablModel	1	ABL model type (1: Nieuwstadt, 2: .nc/.dat input from PALM/TOSCA, requires profiles.nc / ABL_averaging.mat)
bkStateName	tosea	Only required if <code>ablModel = 2</code> (PALM input: palm, TOSCA input: tosea)
displayMicroScale	0	Computes wind field around wind farm (COMPUTATIONALLY EXPENSIVE, for post-processing only)
wakeModelLogLaw	1	Zero: use uniform inflow for wake model RHS, one: use log inflow for wake model RHS
singlePointCoupling	0	If set to one, performs original 3LM one-point coupling
mirrorWindFarm	1	If set to one, mirrors the wind farm w.r.t. the ground
excludeBackground	0	If set to one, excludes background wind variation (corresponds to wake model alone + induction if activated)
ABL Parameters		
ρ	1.225	Reference air density [Kg/m ³]
ν	1.5×10^{-5}	Kinematic viscosity [m ² /s]
g	9.81	Gravitational acceleration [m/s ²]
T_{ref}	300	Reference ground temperature [K]
U_{ref}	9 0	Reference wind vector at hub height [m/s]
H_{ref}	90	Reference hub height [m]
H	500	Reference ABL height [m]
dTH	0 or 4.95	Temperature jump across capping [K]
$dTdz$	0 or 7.7	Lapse rate above capping [K/Km]
$dTdzABL$	0	Lapse rate below capping [K/Km]
z_0	0.0001	Equivalent roughness length [m]
TI	8.94	Turbulence intensity percentage [%]
lat	0	Latitude [deg]
Domain Parameters		
x_s^{Meso}	-200	X mesoscale domain start [Km]
x_e^{Meso}	1200	X mesoscale domain end [Km]
y_s^{Meso}	-100	Y mesoscale domain start [Km]
y_e^{Meso}	100	Y mesoscale domain end [Km]
dx^{Meso}	250	Mesoscale domain discretization in x direction [m]
dy^{Meso}	250	Mesoscale domain discretization in y direction [m]
Wind Farm Parameters		
x_s^{Farm}	0	X farm start [Km]
y_s^{Farm}	0	Y farm start [Km]

farmInputType	3	One: aligned wind farm, two: staggered wind farm, three: read from Excel
excelName	N4.xlsx	Name of the Excel file where turbine coordinates are saved
S_x	5	X turbine spacing in diameters (discarded if <code>farmInputType = three</code>)
S_y	4.7619	Y turbine spacing in diameters (discarded if <code>farmInputType = three</code>)
N_{ty}	5	Number of turbines in Y direction (discarded if <code>farmInputType = three</code>)
N_{tx}	5	Number of turbines in X direction (discarded if <code>farmInputType = three</code>)
D	126	Turbine diameter [m] (discarded if <code>farmInputType = three</code>)
z_{Hub}	90	Turbine hub height [m] (discarded if <code>farmInputType = three</code>)
useTurbineCurves	1	Zero: constant C_t and C_p (below), one: read curves from <code>input/turbineCurves.mat</code> (wind, C_p , C_t tables)
C_t	0.85	Default turbine thrust coefficient (discarded if <code>farmInputType = three</code>)
C_p	0.5	Default turbine power coefficient (discarded if <code>farmInputType = three</code>)

Input for excel:

Excel Column	A	B	C	F	G	H
Name	x-coordinate	y-coordinate	z-coordinate	D	z_{hub}	C_t

D is always 126 m, z_{hub} 90 m and C_T 0.85, but is changed accordingly as explained in Figure 4.2.

Appendix D Comparison between background velocity and streamwise velocity in TNBL and CNBL

In Figure D.1, one sees two methods to show the CNBL effects for a simulation with two wind farms distanced by 39.1D. By subtracting the velocity profiles of the TNBL and CNBL simulation, the CNBL effects are positioned at $y=0$. To make a comparison with the background velocity u^{bk} , the depth-averaged velocity profile over the wind farm layer is added up to the velocity profile subtraction of TNBL and CNBL. The relations are very similar, one sees a global blockage and speed up for both WF1 and WF2. In general one can see that the blockage effects are lower for the background velocity method for both WF1 and WF2. The speed up in WF1 is also a little lower, but the speed up for WF2 is a little bit higher. This difference could affect the velocity analysis.

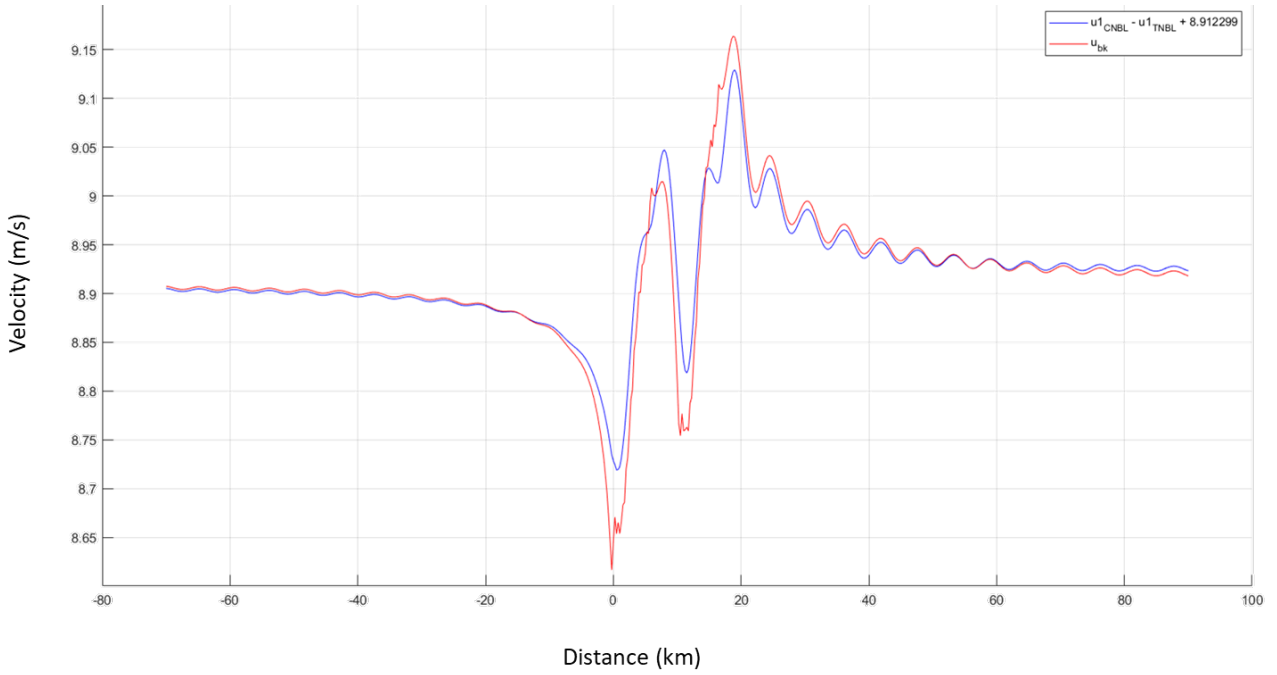


Figure D.1: Background velocity vs streamwise velocity difference TNBL and CNBL